Title

Isotopic fractionation accompanying CO2 hydroxylation and carbonate precipitation from high pH waters at The Cedars, California, USA

Permalink

https://escholarship.org/uc/item/7kf579nr

Authors

Christensen, John N
Watkins, James M
Devriendt, Laurent S
et al.

Publication Date

2021-05-01

DOI

10.1016/j.gca.2021.01.003

Isotopic Fractionation Accompanying CO_2 Hydroxylation and Carbonate Precipitation from High pH Waters at The Cedars, California, USA

John N. Christensen[1*], James M. Watkins[2], Laurent S. Devriendt[3], Donald J. DePaolo[1,4], Mark E. Conrad[1], Marco Voltolini[1], Wenbo Yang[5], and Wenming Dong[1]

[1]Earth and Environmental Science Area, Energy Geosciences Division, Lawrence Berkeley National Laboratory, Berkeley, CA 94720.
[2]Department of Earth Sciences, University of Oregon, Eugene, OR 97403
[3]Royal Netherlands Institute for Sea Research (NIOZ), Landsdiep 4, 1797 SZ 't Horntje, The Netherlands
[4]Department of Earth and Planetary Science, University of California, Berkeley, CA 94720.
[5]Department of Integrative Biology, University of California, Berkeley, CA 94720.
*Corresponding author jnchristensen@lbl.gov

Abstract

The Cedars ultramafic block hosts alkaline springs (pH > 11) in which calcium carbonate forms upon uptake of atmospheric CO_2 and at times via mixing with surface water. These processes lead to distinct carbonate morphologies with “floes” forming at the atmosphere-water interface, “snow” of fine particles accumulating at the bottom of pools and terraced constructions of travertine. Floe material is mainly composed of aragonite needles despite $CaCO_3$ precipitation occurring in waters with low Mg/Ca (<0.01). Precipitation of aragonite is likely promoted by the high pH (11.5-12.0) of pool waters, in agreement with published experiments illustrating the effect of pH on Ca-carbonate polymorph selection.

The Ca-carbonates exhibit an extreme range and approximately 1:1 covariation in $\delta^{13}C$ (−9 to −28‰ VPDB) and $\delta^{18}O$ (0 to −20‰ VPDB) that is characteristic of travertine formed in high pH waters. The large isotopic fractionations have previously been attributed to kinetic isotope effects accompanying CO_2 hydroxylation but the controls on the $\delta^{13}C$-$\delta^{18}O$ endmembers and slope have not been fully resolved, limiting the use of travertine as a paleoenvironmental archive. The limited areal extant of the springs at The Cedars (~0.5 km^2) and the limited water sources, isotopic compositions and temperatures, combined with our sampling strategy and the addition of Ca isotopic measurement, allow us to place tighter constraints on the processes involved in generating the systematic C and O isotope variations.

We develop an isotopic reaction-diffusion model and an isotopic box model for a CO_2-fed solution that tracks the non-equilibrium isotopic composition of each dissolved inorganic carbon (DIC) species and $CaCO_3$. The box model includes four sources or sinks of DIC (atmospheric CO_2, high pH spring water, fresh creek water,

HCO_3^-, pH = 7.8-8.7) that occasionally or locally mixes with the high-pH spring water. The bulk carbonate $\delta^{13}C$ and $\delta^{18}O$ values of modern and ancient travertines therefore reflect the proportion of calcium carbonate formed by processes (1) and (2), with process (2) dominating the carbonate precipitation budget at The Cedars. These results show that recent advances in understanding kinetic isotope effects allow us to model complicated, but common natural processes, and suggest ancient travertine may be used to retrieve past surface water $\delta^{18}O$ and atmospheric $\delta^{13}C$ values. There is evidence that older travertine at The Cedars records atmospheric $\delta^{13}C$ that predates large-scale combustion of fossil fuels.

1. Introduction

Most Earth-surface carbonate minerals precipitate out of stable isotopic equilibrium with their host aqueous solution (Coplen, 2007; Watkins et al., 2013, 2014; Devriendt et al., 2017; Daëron et al., 2019). Deviations from equilibrium are manifested in a variety of ways. One of the most striking ways, still not fully understood, is a strong correlation between $\delta^{13}C$ and $\delta^{18}O$ in carbonates precipitated under different circumstances, from marine calcifying organisms (e.g., McConnaughey, 1989; Spero et al., 1997; Adkins et al., 2003; Kimball et al., 2014; Hermoso et al., 2014; Chen et al., 2018), to cryogenic calcium carbonates (Clark and Lauriol, 1992; Žák et al., 2008), lacustrine carbonates (Talbot, 1990), and speleothem carbonates formed by CO_2 degassing (Daëron et al., 2011; Tremaine et al., 2011). The slope of the $\delta^{13}C$-$\delta^{18}O$ co-variation varies from place to place because each setting is somewhat unique and because kinetic isotope effects in the DIC-H_2O-$CaCO_3$ system are sensitive to factors such as temperature, solution pH, mixing between DIC reservoirs, the residence time of DIC in solution, whether CO_2 is ingassing or outgassing from solution, and whether the system is open versus closed (e.g. McConaughey, 1989; Clark et al., 1992; Falk et al., 2016; Devriendt et al., 2017; Chen et al., 2018).

Ca-carbonates formed in hyperalkaline springs exhibit some of the largest and most systematic variations of $\delta^{13}C$ and $\delta^{18}O$ (O'Neil and Barnes, 1971; Clark and Fontes, 1990; Clark et al., 1992; Meister et al., 2011; Leleu et al., 2016; Falk et al., 2016). The archetype locality is a set of carbonate formations precipitating from springs emanating from serpentinized peridotite in the Samail ophiolite, Sultanate of Oman (Barnes et al., 1978; Clark et al., 1992; Kelemen et al., 2011; Mervine et al., 2014; Falk et al., 2016). Figure 1 (data from Falk et al., 2016; Mervine et al., 2014; Clark et al., 1992; Clark and Fontes, 1990) shows the strong $\delta^{13}C$-$\delta^{18}O$ correlation spanning a range of about 25‰, with most of the values being isotopically lighter than the expected equilibrium value. The isotopically light endmember of the $\delta^{13}C$-$\delta^{18}O$ array has been attributed to hydroxylation of dissolved CO_2 ingassing from the atmosphere (Clark et al., 1992). The rest of the array has been attributed to some combination of mixing between different DIC sources, partial equilibration of DIC, and post-depositional recrystallization (Falk et al., 2016). Recent progress has been made on the development of numerical models that quantify kinetic isotope effects in the DIC-H_2O-$CaCO_3$ system (Devriendt et al., 2017; Sade and Halevy, 2017; Chen et al., 2018), providing an opportunity to gain a more quantitative understanding of the peculiar and large kinetic isotope effects in high pH environments.

The Ca-carbonate samples from Oman represented in Fig. 1 were collected over an area of 50 km x 200 km from calcium-hydroxide springs (pH = 11.2-12.1) spanning a large range in temperature (22-32°C), possibly large range in $\delta^{13}C$ of DIC surface and ground waters, and large range in the age of samples (0 to 40 ka). This is the main reason the range of possible equilibrium calcite values is large (Fig. 1). In this study, we investigate a similar high-pH system, The Cedars, where the springs are within a 0.5 km^2 area, and the spring waters have a more constant temperature (17.4 ± 1°C) and $\delta^{13}C$ composition. Recognizing that kinetic isotope effects are growth-rate-dependent, our approach is to determine the calcite and aragonite growth rates using Ca isotopes and detailed field observations, and produce a dataset where the $\delta^{13}C$ and $\delta^{18}O$ values of the minerals could be evaluated in the context of these growth-rate data and with reference to the growth conditions, travertine forms, and likely controls on CO_2 transport.

2. The Cedars

The Cedars (aka Cazadero e.g. Barnes et al. 1967) peridotite is a relatively small tectonically emplaced fault-bounded wedge of ultramafic rock located in the California Coast Range north of San Francisco (Blake et al 2012, Coleman 2000) (Fig. 2). The dominant rock type is harzburgite with lesser amounts of dunite. This fragment of Jurassic age oceanic lithosphere has been inferred to be an obducted abyssal peridotite from an oceanic fracture zone (Coleman 2000), or alternatively as the basal peridotite of the Coast Range Ophiolite formed in the mantle wedge above the Mesozoic California-margin subduction zone (Choi et al. 2008). The central portion of The Cedars is partially serpentinized, while the margins consist of sheared serpentinite (Blake et al. 2012). The Cedars ultramafic body is in fault contact with Franciscan Complex mélange greywacke and shale (Coleman 2000). It has a dipping, wedge-shaped structural geometry, extending to a depth of 4km but with an average thickness of only 2km or less (Blake et al. 2002).

A series of springs emerge along the course of Austin Creek at the bottom of the main canyon between ~275 m and 335 m elevation. Some springs produce pools and terraced deposits adjacent to the creek before emptying into the creek. At other locations springs enter the creek directly from the bottom. An example at the Barnes Spring Complex (BSC, Fig. 2) of a spring-fed pool adjacent to Austin Creek is shown in Fig. 3. The unusual nature of the springs at The Cedars was first recognized and described by Barnes et al. (1967). They found that the springs produce low-temperature (~18 °C) ultrabasic waters with high pH (11.7), nil carbonate, low Mg, Fe, and silica concentrations but relatively high Ca. They attribute the spring water's unusual chemical characteristics to involvement in on-going serpentinization of primary ultramafic rock at shallow depth (see also Barnes and O'Neil, 1969). A subsequent stable isotopic study demonstrated that the spring waters have a meteoric origin as opposed to an ancient connate origin from the underlying Franciscan formation (Barnes and O'Neil, 1969; Barnes et al. 1978), and that Ca-carbonates precipitating from the ultrabasic waters have unusually low $\delta^{13}C$ and $\delta^{18}O$ values (O'Neil and Barnes, 1971).

Morrill et al. (2013) conducted a more extensive study of the high pH waters of The Cedars. They identified two types of ultrabasic water at The Cedars that variably mix: (1) waters with deep flow-paths that interacted with the underlying Franciscan Complex enriching the waters in K^+, salinity, and volatile organic compounds before encountering ultramafic rock, and (2) waters with shallow paths that pass solely through ultramafic rock and are characterized by lower salinity and $[K^+]$. The springs exhibit stable temperatures with time and season (spring *vs.* fall), averaging about 17±1˚C (Morrill et al., 2013; Suzuki et al., 2013). Tritium dating of water samples by Suzuki et al. (2017) indicates that water with deep flow paths, as at the Grotto Pool Springs, has an age greater than 60 years (<0.8 Tritium units, TU), while Barnes Complex spring water, with an inferred shallow flow path, gave a value of 2.3 TU, possibly indicating an age younger than 10 years since that value is similar to contemporaneous Bay Area precipitation (1.3-2.2 TU; Harms 2015).

3. Methods

3.1 Sampling

Samples for this study were collected on eight visits to The Cedars in 2013, 2014, 2016, and 2018. Four sites were sampled (Fig. 2): (1) The Wedding Cake above Mineral Falls, (2) The Barnes Spring Complex (BSC), (3) Grotto Pool Springs (GPS), and (4) "New" Pool within Austin Creek ~ 250m upstream of BSC. Water samples from the high pH springs and from Austin Creek were filtered to 0.22 μm using Durapore filter units (Millipore), collected in HDPE bottles and acidified to pH 2 using high purity HNO_3 (Baseline Nitiric Acid, Seastar Chemicals). Prior to collection, the pH of the sampling source was measured with an Orion hand-held pH meter

(Thermo Scientific). Samples of Ca-carbonate collected are of several types as illustrated in Fig. 3: (1) partially consolidated material from rims of pools (e.g. Wedding Cake); (2) precipitates from the surfaces of pools (called here floes); (3) dendritic forms and encrustations from sites of creek-spring mixing; (4) unconsolidated material (called here snow) from pool bottoms; and (5) solid, old travertine deposits (sample collected at BSC). Surface floes were either skimmed from the surface or captured on screens.

3.2 Analytical Methods

Below are given brief descriptions of the analytical techniques used in this study. Further details are provided in the Supplement.

Samples of Ca carbonate and water were analyzed for Ca isotopic composition using thermal ionization mass spectrometry on a Triton (mfd. by ThermoFisher) multicollector instrument. Prior to chemical separation, samples were spiked with a double ^{42}Ca-^{48}Ca double spike. The Ca isotope results are reported as per mil deviations of the ^{44}Ca/^{40}Ca ratio (δ^{44}Ca) from Bulk Silicate Earth (BSE) (Nielsen et al. 2011). We have confirmed with recent measurements that our BSE reference ^{44}Ca/^{40}Ca ratio is 0.96±0.05‰ higher than the value for SRM915a.

Oxygen and carbon isotopic analyses of carbonate samples were conducted in the Center for Stable Isotope Biogeochemistry (CSIB), Department of Integrative Biology, University of California, Berkeley, using a GV IsoPrime mass spectrometer equipped with Dual-Inlet and MultiCarb systems. Results are reported relative to VPDB (Vienna Pee Dee Belemnite). The overall external analytical precision is ± 0.05‰ for δ^{13}C and ±0.07‰ for δ^{18}O.

Elemental compositions (metal concentrations) of the water samples were determined by Quadrupole-ICPMS (Elan DRC II, PerkinElmer SCIEX, USA). Images of Ca-carbonate samples were obtained with a Zeiss EVO-LS10® microscope, with capabilities of secondary electrons (SE) imaging and back-scattered electrons (BSE) imaging. Phase identification and quantification in selected solid samples were carried out via X-Ray powder diffraction with a Rigaku SmartLab® X-ray diffractometer.

4. Results

4.1 XRPD and SEM observations

Fourteen carbonate samples were selected for powder XRPD analysis to cover the observed range in sample texture. The fractions of the identified mineral phases are given in Table 1. Material from pool edges ranges from 99.7% aragonite (Wedding Cake) to 46.6% aragonite (BSC Pool B). Aragonite and/or calcite are found in all samples, with aragonite ranging from 18% to 99.7%, and calcite ranging from 0.14% to 82%. Small amounts of vaterite (a polymorph of Ca carbonate) were identified in one floe sample (BSC Carb I, 0.5 ± 0.2%) and in one sample of a pool edge (BSC PE-C2 "crust" 0.6 ± 0.2%). Brucite ($Mg(OH)_2$) was found in some samples of BSC pool edges (PB-C2, PE-C2 3 and 8%, respectively) in a filtered snow sample from BSC (PB-1 6.8%), from a GPS pool (Carb K 0.5%), and in one of the samples from mixed spring-creek water (Carb AA 7.7%). In samples of snow filtered from GPS pool water both hydromagnesite (Carb J 27%; Carb K 49.5%) and nitromagnesite (Carb J 4.5%; Carb K 2.3%) are detected. Nesquehonite ($MgCO_3 \cdot 3H_2O$) was also detected in one sample (3% in Carb K).

The sample of the rim of the Wedding Cake (Carb A) was at collection relatively firm, yet still friable. The SEM images of the material (Fig. S1) show elongate crystals up to 10-15 μm of aragonite (as identified by the XRPD analysis) gathered in bundles, sprays and spheres. The samples from the New Pool (Carb B and Carb C) affected by creek mixing, is also identified by XRPD as 100% aragonite, and consist of sharp needles of aragonite up to at least 40 μm grouped in radial sprays or spheres (Fig.s S2 and S3). Both the soft encrustation on rock and the elongate branching forms display similar micro-textures.

The samples of floes have a more varied mineralogy and texture than samples from the Wedding Cake and from the New Pool. Figure 4 compares the inferred top (upwards from water) and bottom (down into the water) surfaces of floe Ca-carbonates from a BSC pool. The inferred top-side of the floe (Fig. 4A) displays radiating horizontal sprays of aragonite crystals, forming a relatively flat surface. In contrast, the inferred bottom side (Fig. 4B) is rougher, with the terminations of the aragonite sprays forming a hummocky surface. Calcite rhombohedra are scattered across this surface, apparently forming largely after growth of the aragonite sprays. Open areas constitute approximately 15-20% of the area of this floe sample (Carb. D). Fig. S4 in the Supplement provides views of the broken edges of this floe material (Carb D). In the cross-sections the aragonite sprays can be seen to radiate from points, forming intersecting hemispheres. In this case the floe has a thickness of about 10 to 12 μm. Similar differences between the tops and bottoms of floes are confirmed by examination of carefully collected samples so that flakes of known original orientation could be examined by SEM (Fig. 4C).

The growth rate of the floes was determined by measuring the thickness as a function of time. After eight days of Ca-carbonate growth, floe thickness was 20 to 25 μm, as determined using SEM images of oriented fragments (Fig. 5). In the inset to Fig. 5, a piece of floe collected after four days of growth shown at the same scale has half the thickness of the eight-day growth, suggesting a constant linear growth rate of about 3 μm/day.

Sparse florets of hydromagnesite (identified by EDS and morphology) can be found at or partially embedded into the surfaces of calcite rhombs (Suppl. Fig. S5), indicating that hydromagnesite is a trace and late-precipitating phase but can be contemporaneous with calcite growth. Other observed features include co-occurring smooth calcite rhomb faces together with rough micro-stepped saddles (Supp. Fig. S6) suggestive of the effects of bacterially exuded bio-polymers (e.g. Lian et al. 2006; Tourney and Ngwenya 2009), associations with apparent bacterial colonies (Supp. Fig. S7) and aragonite needles featuring stacked steps of hexagonal plates (Supp. Fig. S8) that are suggestive of surface nucleation control of growth.

From the above observations, we infer the following growth stages for floes forming at the surface of high pH pools:

1. Nucleation of aragonite crystals, with horizontal sprays of aragonite crystals suspended by surface tension and forming the base for layer formation.

2. Bundles of aragonite crystals grow parallel to the water surface and downward into the water, forming hemispheres of crystals that merge to form a nearly continuous layer.

3. After aragonite, blocky rhombohedral calcite crystals form, nestled among aragonite hemispheres. Calcite can be seen overgrowing aragonite needles.

4. Late, but accompanying calcite growth, precipitation of hydromagnesite, $Mg_5(CO_3)_4(OH_2)\cdot 4H_2O$) (or perhaps a different hydrous Mg-carbonate (Dypingite $Mg_5(CO_3)_4(OH_2)\cdot 5H_2O$)).

5. Eventually the floe sinks to the bottom of the pool when a mechanical disturbance breaks the surface tension. See the Supplement for a discussion of the limits of surface tension on floe thickness. After sinking to the bottom of the pool, calcite growth can continue, decorating the broken edges of the floe fragments.

4.2 Chemistry of water samples

The concentrations of selected elements in the water samples along with pH are presented in Table 2. The direct samples of springs and of pools have pH in the range of 11.3 to 12, and are characterized by high Ca concentrations (12 to 58 ppm), high K concentrations (0.5 to 7 ppm), and low Mg concentrations (0.07 to 0.35 ppm). In contrast, samples of Austin Creek have pH in the range of 7.8 to 9.5 and are characterized by relatively low Ca concentrations (1.2 to 8 ppm), low K (0.06 to 0.7 ppm) and high Mg concentrations (41 to 49 ppm). The pool and spring water samples with pH $\geq$ 11.3 mostly have very low Mg/Ca molar ratios, less than 0.01, except for two samples of the Wedding Cake pool that have Mg/Ca ratios of 0.34 and 4.5. The creek samples have high Mg/Ca ranging from 8.5 to 66, which varies with pH, suggesting mixing between surface water with high Mg/Ca (pH 7-9) with low Mg/Ca spring water (11-12). Mixing models between creek water and spring water fit well the water samples with pH <11 (Fig. 6), indicating that the chemical influence of spring water can be discerned in downstream creek samples.

4.3 Ca isotopic compositions of water samples

The high pH water samples range in δ^{44}Ca from 0.02‰ up to 1.23‰. The low end of the range is similar to the δ^{44}Ca of upper mantle peridotite (Huang et al., 2010) consistent with the Ca in the springs being derived from the serpentinization of the ultramafic rocks. The sample with the highest Ca concentration (58 ppm, Wedding Cake Seep) also has the lowest δ^{44}Ca (0.02±0.06‰), while the sample with the lowest Ca concentration (12 ppm, Wedding Cake Pool) has the highest δ^{44}Ca (1.23±0.06‰). This pattern in concentration and δ^{44}Ca suggests an effect due to precipitation of Ca-carbonate at the various sampling localities and times. To examine this, the isotopic data for the waters with pH > 11 (F1-F4, F7-F15) are used for Rayleigh distillation calculations, the results of which are shown in Fig. 7A. The slope of the best-fit line to the data ($r^2 = 0.91$, $p < 0.01$) gives a Δ^{44}Ca of -0.76 ± 0.12‰ (95% confid.), indicating that this is the average Ca isotopic fractionation accompanying the removal of Ca^{2+} to Ca-carbonate from the various waters at The Cedars. Below we compare this value to results for Δ^{44}Ca derived from direct water/Ca-carbonate differences.

4.4 Calcium isotopic compositions of Ca-carbonate

The Ca isotope compositions of the measured Ca-carbonates fall in a relatively narrow range of δ^{44}Ca from -0.77‰ to -0.17‰ (Table 3), with no correlation with either δ^{13}C or δ^{18}O (see Supplement Fig. S9). The analyzed Ca-carbonates cover a range of textures and mineralogy. Because of their immediate association with water, the floe samples provide the best opportunities to directly measure fractionation (Δ^{44}Ca) between Ca-carbonate and dissolved Ca^{2+} arising from crystallization. We analyzed five water-floe pairs (Table 4), three from different pools at the BSC, and one each from the Wedding Cake and from the GPS. The average of all five pairs gives a Δ^{44}Ca of -0.75±0.07‰ that compares well to the value given above from the Rayleigh distillation calculation (Fig. 7B).

4.5 $\delta^{18}O$ and $\delta^{13}C$ of Ca-carbonate samples

The $\delta^{18}O$ and $\delta^{13}C$ data are presented in Table 3 and Tables S1-S3 in the Supplement, and displayed in Fig. 8 along with data for Ca-carbonates from The Cedars analyzed by Meister et al. (2011). The $\delta^{18}O$ and $\delta^{13}C$ values of the Ca-carbonates of all textures fall along a roughly 1:1 line, far from the expected composition for Ca carbonate in equilibrium with Cedars water ($\delta^{18}O \sim -6$ ‰ VPDB). This 1:1 array stretches from highly fractionated, low values of $\delta^{13}C$ and $\delta^{18}O$ toward, but not reaching, the composition of atmospheric CO_2. These characteristics of the $\delta^{18}O$ and $\delta^{13}C$ data, which have been observed also in other alkaline springs associated with ultramafic rocks (e.g. Clark et al. 1992, Leleu et al. 2016, Falk et al. 2016) are explored in the modeling described in the discussion below. The Ca-carbonate samples with the lowest $\delta^{18}O$ and $\delta^{13}C$ values are floes from BSC. Other floe samples from GPS fall further up the array, while a floe sample from the Wedding Cake pool is near the high end of the array. Ca-carbonate of different occurrences (textures), pool rim material, and snow from pool bottoms, have compositions distributed along the array. The samples from the Wedding Cake (floe and rim materials) are displaced to the left of the main array, while samples of old laminated carbonates (travertine) form a separate parallel array displaced to the right. Samples of snow from a GPS pool (Carb J, Table 2; GPS-1 #1-3, Suppl. Table S1) have the highest $\delta^{18}O$ of all Ca-carbonate samples.

5. Discussion

5.1 Floe growth rate

The sample of floe material collected after eight days of growth (Fig. 5) had a thickness of ~20 μm and provides a constraint on the growth rate of calcium carbonate precipitation represented by floe formation on pool surfaces. The rate of Ca-carbonate growth per square meter is provided by Eq. 1:

$$R\ (\mathrm{mol/m^2/s}) = (d \cdot \rho)/(M \cdot t) \qquad \text{Eq. 1}$$

Where d is the floe thickness (meters), ρ is the floe density (g/m^3) taking into account porosity and the proportions of calcite and aragonite, M is the molecular weight of Ca-carbonate (100.086 g/mole), and t is the time interval of growth (seconds). Given a thickness of ~ 20 μm, a growth time of eight days, a porosity of 0 to 40% (Fig. 4), and a mineral composition of 80% calcite and 20% aragonite, Eq. 1 yields a growth rate range of 4.8×10^{-7} mol/m^2/s to 8.0×10^{-7} mol/m^2/s. From this range in growth rate, an estimate can be made of the aragonite saturation state (Ω) through the equation $R = k(\Omega\text{-}1)^n$ where the rate constant k is given for aragonite precipitation by the empirical relation $\ln(k) = 11.54 - 8690/T$ (T = temp. in Kelvin) and the reaction order, n, is 1.7 (Romanek et al. 2011). Applying this equation to the observed growth range above for a temperature of 17.4°C (Morrill et al., 2013) yields a Ω of ~ 9 to 13. This compares well with the Ω estimates made by Morrill et al. (2013) of 13 for BSC (where our growth rate was measured) and 5 for GPS based on measured ion chemistry.

The calculated range in growth rate, along with the average apparent $\Delta^{44/40}$Ca value of -0.75 ± 0.07‰ derived above is plotted in Fig. 9 for comparison to the experimental data of Tang et al. (2008), to experimental data from Watkins et al. (2017), to data for calcite from natural travertine deposition (Yan et al 2016), and to a theoretical surface reaction kinetic model of DePaolo (2011). The result for The Cedars compares well with the experimental data. The field experiments of Yan et al. (2016) for calcite precipitation on plexiglass slides reached faster growth rates (~ 3 to 6×10^{-6} cm^2/s) in the case of their canal site and yielded a $\Delta^{44/40}$Ca, again consistent the experimental data and model (Fig. 9). However their experiments in pools yielded lower precipitation rates and less negative $\Delta^{44/40}$Ca that fall well below the result for The Cedars for a similar growth rate.

The inferred growth rate for floe Ca-carbonate has implications for the rate of spring resupply to pools, in particular the main BSC pool. For a Ca concentration of 51.7 ppm in the spring water supply of the pool, the growth of each square centimeter of floe to a thickness of 25 μm would require between 43 and 53 ml (depending on density/porosity of the floe) of BSC spring water. The pool water beneath floes represented by samples D, E, F and I had a calcium concentration of 51.1 ppm that is indistinguishable from the BSC spring sample taken at that time (51.7 ppm). Given the area of the pool (roughly 1.6 m^2), a supply rate of fresh spring water to the pool of ~1 ml/s (or ~85 L/day) would be required in order to maintain both the Ca concentration and Ca isotopic composition. At the Wedding Cake pool, evidently the supply of fresh spring water can be limited relative to Ca-carbonate precipitation, since at times the Ca concentration can be driven down by a factor of ~5 relative to the spring source, and the Ca isotopic composition of the pool can be fractionated (fluid F3 δ^{44}Ca = 1.23‰) by Ca-carbonate precipitation.

The Ca-carbonate growth rate inferred above is comparable to the expected flux of CO_2 from the atmosphere to the pool water. In a set of $BaCO_3$ precipitation experiments at pH = 10 using a hydroxide buffer, Usdowski and Hoefs (1986) measured a CO_2 flux of 4.7×10^{-7} mol/m^2/s, which compared well to their own calculated estimate based on CO_2 diffusivity in water and the $CO_{2(aq)}$ hydroxylation rate constant. The similarity between this value at pH 10 and our growth rate estimates for samples precipitated at pH > 10 suggests that Ca-carbonate floe precipitation and uptake of atmospheric CO_2 are coupled (see the modeling discussion below).

5.2 Aragonite precipitation

We observed aragonite in all of our samples examined with XRPD or SEM, as did Meister et al. (2011) and O'Neil and Barnes, (1971), including in pool rims, pool snow, pool floes and precipitates from mixed spring/creek waters (Table 1, Fig. 4 and 5, Fig. S1-S4). Meister et al. (2011) propose that aragonite at The Cedars is associated with high Mg/Ca molar ratios of the water resulting from mixing of high Mg/Ca ratio creek water with the low Mg/Ca spring water leading to a high enough Mg/Ca ratio to inhibit the precipitation of calcite in favor of metastable aragonite. Several direct observations argue against high Mg/Ca as the explanation for all occurrences of aragonite at The Cedars. The pools at the BSC produce floes of aragonite/calcite from solutions with very low Mg/Ca ratios (<0.01, see above and Table 2), with aragonite as the first phase to precipitate followed by calcite (Fig. 4). Likewise, the rims and snow of low Mg/Ca spring pools also contain aragonite. The high pH of spring pools is sensitive to additions of creek water with a pH of 7.8-8.7. Mixing models demonstrate that even with the addition of creek water with Mg/Ca

= 21.8, the Mg/Ca of the mixture does not rise above 2 until the pH falls well below 11 (Fig. 6). Such pH values are not seen in the Ca-carbonate precipitating spring pools (pH range 11.3-12.0, Table 2). However, there are instances of aragonite occurring at locations where spring water enters the creek directly (e.g. Carb B and Carb C, see Suppl. Figs S2 and S3) where high Mg/Ca may play a role in favoring aragonite over calcite. Such samples, precipitating from clearly mixed spring/creek water (Carbs B and C in Table 3; Carbs S, T, Y and AA in Table S1; Samples labeled "mixed Spr/Cr" in Fig. 7), have C and O isotope compositions distinct from aragonite/calcite samples precipitated from spring water.

Alternative chemical variables that potentially can promote aragonite precipitation over calcite from cool springs include high pH and the degree of oversaturation (see review by Jones, 2017). Experiments by Tai and Chen (1998) demonstrate that the favored Ca-carbonate polymorph is a function of solution pH. They found at 24˚C that with pH below 10-10.5, vaterite is the favored polymorph to crystallize, while at pH $\geq$ 12-11.8 calcite is dominant, and for pH in the range of 10.5-11.5 aragonite was the dominant polymorph peaking in abundance at pH $\sim$11.3. Similar effects of pH on Ca-carbonate polymorphism were found by Matsumoto et al. (2010). The degree of supersaturation has been shown by Kawano et al. (2009) to control polymorphism, with high ($\Omega > 15$ at 20˚C) saturation favoring vaterite and at $\Omega < 15$ favoring calcite. However, these experiments were likely conducted at circum-neutral pH (the pH conditions were measured but not given by Kawano et al., 2009) and so may be consistent with the experiments of Tai and Chen (1998) in which at a Ω of $\sim$ 40 and pH < 10 vaterite precipitation was favored. A pH effect on Ca-carbonate polymorphism has also been described for low temperature (0˚C) precipitation of Ca-carbonate; ikaite (a hexahydrate of Ca carbonate) results at pH 13.4 while at pH 9 vaterite is the sole product, regardless of Ca^{2+}/CO_3^{2-} ratio (Hu et al. 2015).

From the SEM observations of floes discussed above, the first phase to precipitate is aragonite, followed by calcite. This is consistent with the surface layer of the water having a pH of 11.0-11.5 and a Ω of 9-13 favoring the nucleation of aragonite over calcite. As the layer thickens it encounters a pH > 11.5 and calcite begins to nucleate and grow. In considering the preferred nucleation of aragonite in modern seawater, Sun et al. (2015) conclude based on *ab initio* calculations that aragonite is favored over calcite for Mg/Ca ratios in the solution greater than ~2 due to the surface energy effect of Mg incorporation stabilizing aragonite relative to calcite. We speculate that the effect of pH is to change the surface energy of Ca-carbonate nuclei such that the aragonite nucleation rate is maximized at pH 11.0-11.5, whereas calcite nucleation and growth is promoted at higher pH.

5.3 Kinetic modeling of oxygen and carbon isotope fractionation

A significant advance of the past decade has been the development of quantitative models of kinetic isotope effects between precipitating Ca-carbonate crystals and dissolved ions (DePaolo, 2011; Nielsen et al., 2012, 2013; Watkins et al., 2013, 2014, 2017; Devriendt et al., 2017) and between DIC species and water (Devriendt et al., 2017; Chen et al., 2018). Chen et al (2018) developed a model that integrates CO_2 transport, fluid mixing, carbonate system reaction kinetics, and carbonate precipitation, a combination that is necessary to understand alkaline springs like those at The Cedars. This model is informed by extensive experimental and theoretical work on the kinetics and isotope fractionations among DIC species (e.g. Usdowski et al., 1991; Clark et al., 1992; Usdowski and Hoefs, 1993; Zeebe and Wolf-Gladrow, 2001; Beck et al., 2005; Kim et al., 2006; Zeebe, 2014; Sade and Halevy, 2017) and carbonate minerals (Romanek et al., 1992; Kim et al., 2007; Wolthers et al., 2012; Watkins et al., 2013, 2014). In this section, we present a model adapted from that of Chen et al. (2018), and use it to evaluate the observed C and O isotopic variations, while also using the constraints we have on carbonate growth rates and Ca isotopic compositions.

HCO_3^- with subsequent rapid and near-quantitative conversion to CO_3^{2-}. The precipitation of Ca carbonate to build the floes consumes much of the DIC coming from the atmosphere. The isotopic composition of the DIC (essentially all in the form of CO_3^{2-}) is set by hydroxylation of the incoming atmospheric CO_2 to extremely low $\delta^{13}C$ and $\delta^{18}O$ values, and remains at such values unless shifted by the addition of DIC from spring water or creek water.

As the floe thickens, it eventually detaches and sinks, carrying with it some of the low $\delta^{13}C$ and $\delta^{18}O$ surface water into the deeper pool. Hence, the deeper pool water from which the "snow" and rim carbonates precipitate obtains some of its DIC from the boundary layer near the surface either by diffusion or by the fluid boundary layer physically detaching, sinking, and mixing with the deep water. Isotopic equilibration of the detached layer is hindered by the high pH of the pool water, so the kinetic signature of the surface processes can be preserved for a long period of time—days to tens of days at pH = 11.5 (Usdowski et al., 1991).

This conceptual framework is used to construct a two-stage model for what is happening at The Cedars (Fig. 11). The first stage, hereafter referred to as the thin-film model, focuses on the diffusional boundary layer (~100 μm) at the pool-atmosphere interface. We solve a system of reaction-diffusion equations to compute the concentrations and isotopic compositions of DIC species throughout the one-dimensional model domain. The results place constraints on the hydroxylation kinetic fractionation factors (note that KFF = $(\alpha\text{-}1)\cdot 1000$), which are used for defining the isotopic composition of the equilibrated inorganic carbon (EIC = HCO_3^- + CO_3^{2-}; Chen et al., 2018) flux in the second stage. The second stage, hereafter referred to as the box model, describes the isotopic composition of a well-mixed reservoir as a function of the following fluxes with distinct isotopic compositions: (1) an EIC flux from the detached surface layer, (2) a spring replenishment flux, (3) a low-pH (8.7) creek flux, and (4) a $CaCO_3$ precipitation flux. The box model also includes reactions among DIC species. The results are used to determine the environmental conditions required to produce the full $\delta^{18}O$-$\delta^{13}C$ data array.

5.3.1 Thin-film model

For the thin-film model, we start with a pool having a pH of 11.5 and a low DIC concentration of ~0.035 mM, based on the value for a BSC water sample given by

Morrill et al. (2013). With these specified pH and DIC values, all other carbonate parameters are calculated based on expressions given by Zeebe and Wolf-Gladrow (2001) and pK values from Millero et al. (2006). The pool is assumed to be isotopically equilibrated initially (Table 5) and at saturation with respect to calcite ($\Omega = 1$), from which we calculate an initial Ca^{2+} concentration of 1.3 mM, in the range of 0.94 to 1.3 mM reported by Morrill et al. (2013).

The rate of CO_2 uptake from the atmosphere is determined by the contrast between the partial pressure (or fugacity) of the atmospheric CO_2 and the concentration of $CO_{2(aq)}$ in the surface water of the pool. The exchange across the surface between the gas phase CO_2 and the water is assumed to be very fast in comparison to the diffusive transport of the CO_2 into the pool away from the surface; i.e., local equilibrium:

$$[CO_2]_{\mathrm{interface}} = K_0 \cdot f_{CO2}, \qquad \text{Eq. 2}$$

where K_0 is Henry's constant (mol/kg-soln/atm) and f_{CO2} is the fugacity of CO_2 (atm). For a 400 ppm atmosphere, this leads to $[CO_2]_{eq} = 1.6 \times 10^{-5}$ moles/kg-soln which is several orders of magnitude higher than the concentration in the bulk pool. The incoming CO_2 is converted to HCO_3^- according to the following reactions (cf. Chen et al. 2018):

$$CO_2 + H_2O \underset{k_{-1}}{\overset{k_{+1}}{\rightleftarrows}} HCO_3^- + H^+ \qquad \text{Reaction 1}$$

$$CO_2 + OH^- \underset{k_{-4}}{\overset{k_{+4}}{\rightleftarrows}} HCO_3^- \qquad \text{Reaction 2}$$

$$^{13}CO_2 + H_2O \underset{k'_{-1}}{\overset{k'_{+1}}{\rightleftarrows}} H^{13}CO_3^- + H^+ \qquad \text{Reaction 3}$$

$$^{13}CO_2 + OH^- \underset{k'_{-4}}{\overset{k'_{+4}}{\rightleftarrows}} H^{13}CO_3^- \qquad \text{Reaction 4}$$

$$CO_2 + H_2{}^{18}O \underset{1/3a_{-1}}{\overset{a_{+1}}{\rightleftarrows}} HC^{18}OO_2^- + H^+ \qquad \text{Reaction 5}$$

$$CO_2 + {}^{18}OH^- \underset{1/3a_{-4}}{\overset{a_{+4}}{\rightleftarrows}} HC^{18}OO_2^- \qquad \text{Reaction 6}$$

$$C^{18}OO + H_2O \underset{2/3b_{-1}}{\overset{b_{+1}}{\rightleftarrows}} HC^{18}OO_2^- + H^+ \qquad \text{Reaction 7}$$

$$C^{18}OO + OH^- \underset{2/3b_{-4}}{\overset{b_{+4}}{\rightleftarrows}} HC^{18}OO_2^- \qquad \text{Reaction 8}$$

Rate constants for the ^{18}O substituted species are represented by *a* for substitution on H_2O or OH^-, and represented by *b* for substitution on CO_2. The factors of 1/3 and 2/3 are necessary for oxygen isotope mass balance. For every mole of $HC^{18}OO_2^-$ that undergoes dehydration, 2/3 goes to $C^{18}OO$ and 1/3 goes to $H_2{}^{18}O$. Hence, the rate of change of $H_2{}^{18}O$ is proportional to 1/3 of the concentration of $HC^{18}OO_2^-$. The same logic applies to the reverse reaction, and a similar argument can be made for the (de-)hydroxylation reactions involving $HC^{18}OO_2^-$. The ratios of forward to backward rate constants are equal to the equilibrium constant for each reaction, as given in Table 6.

At high pH (>11), the hydroxylation reactions are much faster than hydration reactions because OH^- concentration is high. We nevertheless retain the hydration reactions for completeness. The increase in CO_2 and HCO_3^- at the surface establishes large concentration gradients that drive diffusion of DIC species downward through the thin film. At the base of the thin film ($z = -100$ μm), we assume the pool is well-mixed and able to maintain fixed concentrations of dissolved species. For simplicity we assume that all dissolved species diffuse at the same rate and that there is no isotopic fractionation by diffusion (Zeebe, 2011).

The combined process of reaction and diffusion is modeled by solving the following system of partial differential equations:

$$\frac{\partial[CO_2]}{\partial t} = D_{CO_2} \cdot \frac{\partial^2[CO_2]}{\partial z^2} + \{-k_{+1}[CO_2] + k_{-1}[EIC] \cdot x \cdot [H^+]$$
$$- k_{+4}[CO_2][OH^-] + k_{-4}[EIC] \cdot x\} \qquad \text{Eq. 3}$$

$$\frac{\partial[\mathrm{EIC}]}{\partial t} = D_{\mathrm{EIC}} \cdot \frac{\partial^2[\mathrm{EIC}]}{\partial z^2} + \{k_{+1}[\mathrm{CO_2}] - k_{-1}[\mathrm{EIC}] \cdot \chi \cdot [\mathrm{H^+}] + k_{+4}[\mathrm{CO_2}][\mathrm{OH^-}] - k_{-4}[\mathrm{EIC}] \cdot \chi\} \tag{Eq. 4}$$

$$\frac{\partial[\mathrm{Ca^{2+}}]}{\partial t} = D_{\mathrm{Ca}} \cdot \frac{\partial^2[\mathrm{Ca^{2+}}]}{\partial z^2} - \mathrm{Sp} \cdot F_{\mathrm{CaCO_3}} \tag{Eq. 5}$$

$$\frac{\partial[\mathrm{Alk}]}{\partial t} = D_{\mathrm{Ca}} \cdot \frac{\partial^2[\mathrm{Alk}]}{\partial z^2} - 2 \cdot \mathrm{Sp} \cdot F_{\mathrm{CaCO_3}} \tag{Eq. 6}$$

$$\frac{\partial[^{13}\mathrm{CO_2}]}{\partial t} = D_{\mathrm{CO_2}} \cdot \frac{\partial^2[^{13}\mathrm{CO_2}]}{\partial z^2} + \{-k'_{+1}[^{13}\mathrm{CO_2}] + k'_{-1}[^{13}\mathrm{EIC}] \cdot {}^{13}\chi \cdot [\mathrm{H^+}] - k'_{+4}[^{13}\mathrm{CO_2}][\mathrm{OH^-}] + k'_{-4}[^{13}\mathrm{EIC}] \cdot {}^{13}\chi\} \tag{Eq. 7}$$

$$\frac{\partial[^{13}\mathrm{EIC}]}{\partial t} = D_{\mathrm{EIC}} \cdot \frac{\partial^2[^{13}\mathrm{EIC}]}{\partial z^2} + \{k'_{+1}[^{13}\mathrm{CO_2}] - k'_{-1}[^{13}\mathrm{EIC}] \cdot {}^{13}\chi \cdot [\mathrm{H^+}] + k'_{+4}[^{13}\mathrm{CO_2}][\mathrm{OH^-}] - k'_{-4}[^{13}\mathrm{EIC}] \cdot {}^{13}\chi\} + \mathrm{Sp} \cdot F_{\mathrm{CaCO_3}} \cdot \frac{[^{13}\mathrm{EIC}]}{[\mathrm{EIC}]} \cdot ({}^{13}\alpha_{\mathrm{CaCO_3-EIC}}) \tag{Eq. 8}$$

$$\frac{\partial[\mathrm{C^{18}OO}]}{\partial t} = D_{\mathrm{CO_2}} \cdot \frac{\partial^2[\mathrm{C^{18}OO}]}{\partial z^2} + \{-b_{+1}[\mathrm{C^{18}OO}] + \tfrac{2}{3}b_{-1}[^{18}\mathrm{EIC}] \cdot {}^{18}\chi \cdot [\mathrm{H^+}] - b_{+4}[\mathrm{C^{18}OO}][\mathrm{OH^-}] + \tfrac{2}{3}b_{-4}[^{18}\mathrm{EIC}] \cdot {}^{18}\chi\} \tag{Eq. 9}$$

$$\begin{aligned}\frac{\partial[^{18}\mathrm{EIC}]}{\partial t} = D_{\mathrm{EIC}} \cdot \frac{\partial^2[^{18}\mathrm{EIC}]}{\partial z^2} &+ \{a_{+1}[\mathrm{CO_2}]r_{\mathrm{w}} - \tfrac{1}{3}a_{-1}[^{18}\mathrm{EIC}] \cdot {}^{18}\chi \cdot [\mathrm{H^+}] \\ &+ a_{+4}[\mathrm{CO_2}][^{18}\mathrm{OH^-}] - \tfrac{1}{3}a_{-4}[^{18}\mathrm{EIC}] \cdot {}^{18}\chi \\ &+ b_{+1}[\mathrm{C^{18}OO}] - \tfrac{2}{3}b_{-1}[^{18}\mathrm{EIC}] \cdot {}^{18}\chi \cdot [\mathrm{H^+}] \\ &+ b_{+4}[\mathrm{C^{18}OO}][\mathrm{OH^-}] - \tfrac{2}{3}b_{-4}[^{18}\mathrm{EIC}] \cdot {}^{18}\chi\} \\ &+ \mathrm{Sp} \cdot F_{\mathrm{CaCO_3}} \cdot \frac{[^{18}\mathrm{EIC}]}{[\mathrm{EIC}]} \cdot ({}^{18}\alpha_{\mathrm{CaCO_3-EIC}})\end{aligned} \tag{Eq. 10}$$

where D_i is the diffusivity of species i, χ is the fraction of EIC that is $\mathrm{HCO_3^-}$, F_{CaCO3} is the growth rate of $\mathrm{CaCO_3}$ (mol/m^2/s), Sp is the specific reactive surface area (m^2/kg-soln), and r_{w} is the $^{18}\mathrm{O}/^{16}\mathrm{O}$ of water. Reaction terms are set apart by braces { }. Following Chen et al. (2018), we write $\mathrm{CO_3^{2-}}$ and $\mathrm{HCO_3^-}$ together as EIC, assuming instantaneous isotopic equilibration between these two species because they equilibrate on a timescale of 10^{-7} sec (Zeebe and Wolf-Gladrow, 2001). The pH is calculated in the model at each time step from [DIC] and [Alk], assuming instantaneous pH adjustment to these quantities. The time required to establish steady state in the thin film is short, less than 30 seconds, owing to the small length scale of the domain (Supplement Fig. S11).

Steady state profiles are displayed in Fig. 12. The only parameter we treat as adjustable is the specific reactive surface area (Sp), which dictates the efficiency of $CaCO_3$ precipitation. A large Sp implies many crystal nuclei and/or rough crystal surfaces and leads to lower steady state Ω values because a large precipitation flux prevents DIC accumulation (Fig. 12f). In the absence of any constraints on Sp, we report that Sp ~200 ±100 m^2/kg-soln yields pH, growth rate, and Ω profiles that are most consistent with our estimates based on floe thickness and growth rate calculations (Fig. 12i), but note that a wide range of Sp values (10-1000) can be accommodated by the data.

The CO_2 flux from the atmosphere is governed by the concentration gradient of CO_2, which is very large near the surface since the CO_2 in the water is close to zero (Fig. 12a). The diffusive flux of CO_2 into the deeper pool water is very small because the CO_2 hydroxylates faster than it can diffuse. The increase in DIC and removal of Ca^{2+} to $CaCO_3$ both lower the pH near the surface (Fig. 12k). Although the pH is lower, the degree of calcite supersaturation is highest near the surface (Fig. 12f) because the increase in DIC more than offsets the DIC speciation effects caused by lower pH.

The model accounts for isotopic distillation of reactants as they are converted to products. This is clearly seen in the $\delta^{13}C$ profile for CO_2 (Fig. 12g) where isotopically light CO_2 has been removed by hydroxylation, leaving behind a residual CO_2 pool with very low concentration that is extremely isotopically heavy. The abrupt return to the initial value at $z = -100$ is a consequence of the fixed concentration boundary condition in the model. Isotopic distillation does not occur for the $\delta^{18}O$ of CO_2 (Fig. 12d) because the KFF is set at 0‰, as discussed further below.

5.3.2 CO_2 hydroxylation KFFs

The thin-film model is used to inform our estimates of the kinetic fractionation factors (KFFs) related to $CO_{2(aq)}$ hydroxylation, which represents the instantaneous isotopic fractionation between the reactant $CO_{2(aq)}$ (for carbon KFF) or '$CO_{2(aq)}$ + OH^-' (for the bulk oxygen KFF) and the product HCO_3^-. To begin, it is important to note that the hydroxylation reaction is essentially unidirectional in the upper 60 μm of the model domain, where the ratio of forward to backward reaction rates is >1000 (Fig. 12c). This implies that the full kinetic fractionation is expressed in the EIC prior to it being converted to $CaCO_3$. There is, however, an additional kinetic fractionation attending the $CaCO_3$ precipitation reaction that depends on the degree of supersaturation through an equilibration index E_c (Devriendt et al., 2017). Since the degree of supersaturation is relatively modest for Sp > 10 m^2/kg, the precipitation reaction is bi-directional and the precipitating $CaCO_3$ is isotopically heavier than CO_3^{2-}. This drives the isotopic composition of EIC to an isotopically lighter composition than that set by the kinetic limit of hydroxylation (Fig. 12e, h, and l),

The best-fit hydroxylation KFFs depend on the degree of distillation of EIC as it is converted to $CaCO_3$, which in turn depends on Sp (Fig. 12e and 12h). A small Sp leads to a small fraction of the CO_3^{2-} converting to $CaCO_3$. In this scenario, the dissolved CO_3^{2-} records the KFF and the $CaCO_3$ is offset to heavier values (Fig. 12l). By contrast, for Sp > 100, most of the CO_3^{2-} is converted to $CaCO_3$ and in this scenario, the $CaCO_3$ records the KFF while the CO_3^{2-} is offset to even lighter values (Fig. 12l). It may be significant that the one measurement of $\delta^{13}C$ of BSC pool water DIC gives a value of –31.5‰ (VPDB; Morrill et al., 2013), which is about 5‰ lighter than the lightest values recorded by the $CaCO_3$ and consistent with near complete conversion of CO_3^{2-} to $CaCO_3$. This suggests that, instead of the EIC, it is the solid $CaCO_3$ that records the KFF. If indeed there is a near quantitative transfer of the EIC to $CaCO_3$, the carbon and oxygen KFFs estimated from the $\delta^{18}O$ and $\delta^{13}C$ of floe samples should be unaffected by their varying proportions of calcite versus aragonite.

Using the $\delta^{13}C$ values of floes at BSC and of local atmospheric CO_2 for the period 2013-2018 (NOAA CO_2 station Trinidad Head, USA- White et al. 2015), the carbon KFF related to CO_2 hydroxylation is estimated here to be –18.1 ±0.8‰ relative to $CO_{2(aq)}$. Following the same reasoning as for carbon isotopes, a bulk oxygen KFF is estimated at -0.4 ±1.5‰ relative to '$CO_{2(aq)}$+OH^-'. The oxygen KFF calculated relative to '$CO_{2(aq)}$+OH^-' relies on the accuracy of the OH^-/H_2O oxygen EFF. A value of -21.3 ±2.2‰ relative to H_2O for the equilibrium isotopic composition of OH^- was used based on quantum-chemical calculations (Zeebe, 2020). Since the isotopic composition of H_2O can be directly measured with high accuracy, and since the OH^-/H_2O oxygen EFF is likely to get refined in the future, we also report the KFF relative to the sum of '$CO_{2(aq)}$ + H_2O' (KFF* = –7.1 ±0.8‰).

Kinetic isotope effects of similar magnitude have also been reported for a range of natural and synthetic carbonates formed in high pH solutions with gaseous CO_2 as the main DIC source (Table 7). We reviewed the literature on carbonate minerals precipitated from gaseous CO_2 in high pH solutions to compile a set of carbon and oxygen KFFs within a consistent framework. The revised KFF values listed in Table 7 were calculated by taking into consideration the following:

(i) The temporal and geographical variability in the $\delta^{13}C$ and $\delta^{18}O$ of atmospheric CO_2 (Trolier et al., 1996; Keeling et al., 2001) for studies where the DIC source was atmospheric CO_2.

(ii) $CO_{2(g)}$ distillation effects were corrected for in (semi-)closed system experiments while an infinite $CO_{2(g)}$ pool was assumed for fully open experiments.

(iii) Values for the equilibrium fractionation factors (EFFs) between $CO_{2(aq)}$ and $CO_{2(g)}$ of -1.1‰ and -0.3‰ were applied for carbon (Vogel et al., 1970) and oxygen (Beck et al., 2005; Barkan and Luz. 2012) isotopes, respectively.

For carbon isotopes, laboratory experiments suggest a KFF between -13.7 ±0.1‰ and -17.2 ±0.6‰ (Table 7, Fig. 13a, Craig, 1953; Usdowski and Hoefs, 1986; Clark et al., 1992; Dietzel et al., 2009; Böttcher et al., 2018) while field data suggest a very consistent KFF of between -16.9 ±1.3‰ and -17.2 ±0.6‰ (Table 7, Fig. 13a; Clark et al., 1992; Mervine et al., 2014; Falk et al., 2016; this study). Some of the disparities could be due to partial re-equilibration (i.e., non-unidirectional hydroxylation reaction), but this is difficult to evaluate. Only three studies suggest a significantly lower carbon KFF than ~ -17‰ (Craig, 1953; open system experiment of Clark et al., 1992; 4°C experiments of Böttcher et al., 2018). Lower apparent KFF may be caused by $CO_{2(g)}$-$CO_{2(aq)}$ disequilibrium when using cold air as a DIC source; Böttcher et al. (2018) conducted their experiments at 4°C while Craig (1953) and Clark et al. (1992) used compressed air (presumably colder than room temperature) in their experiments. Alternatively, the carbon KFF may be negatively correlated with temperature (Fig. 13a, $r^2 = 0.53$, p-value = 0.01), though this hypothesis is not supported by theoretical work (Guo, 2019).

For oxygen isotopes, most studies suggest a bulk KFF close to zero or slightly negative expressed relative to the sum of reactants '$CO_{2(aq)}$ + OH^-' (-2.8 ±1.5‰ to +0.5 ±1.1‰, Clark et al., 1992; Mervine et al., 2014; Falk et al., 2016; Böttcher et al., 2018; this study). However, the experimental work of Clark et al. (1992) and Dietzel et al. (2009) suggests a negative bulk oxygen KFF of between -10.0 ±0.9‰ and -7.9 ±0.8‰. Although the cause of this discrepancy is unclear, the excellent agreement in the bulk oxygen KFF value among all the field studies and the Böttcher et al. (2018) experimental work at 21˚C suggests an oxygen KFF of -0.2 ±0.7‰ over the 17-28°C temperature range (Fig. 13b). This result is consistent with theoretical calculations for a bulk KFF close to 0‰ (Sade and Halevy, 2017; Guo, 2019).

Over the 17-28°C temperature range, the calculated KFF* values average -6.8 ±0.8‰ when expressed relative to 'CO_2+H_2O' (Fig. 13c). The lower KFF* calculated form the experimental result at 5°C (Bottcher et al., 2018) may indicate a positive temperature effect on the KFF of ~ 0.14‰/˚C but this result will need confirmation with additional data. Such a temperature dependence would be in part caused by the effect of temperature on the OH^-/H_2O oxygen EFF (i.e. ~+0.06‰/°C; Zeebe, 2020).

5.3.3 Box model for the pools

The thin-film model is useful for quantifying the hydroxylation KFFs and understanding the isotopically light end of the array. To understand the overall trend we consider the different sources of DIC and forms of carbonate precipitating in the pools as a whole. Unlike the thin film at the surface, it takes much longer than 30 seconds to establish steady state in the larger volume (10-1000 L) pools. For this part of the system we apply a box model with four fluxes representing the sources and sinks of DIC: (1) an atmospheric flux, (2) a replenishment flux from the spring, (3) a flux from the adjacent low-pH (8.7) creek, and (4) a Ca carbonate precipitation flux. For the atmospheric flux of DIC to the pool (J_{atm}) we use a value of 6×10^{-7} mol/m^2/s, based on the steady state EIC gradient in the thin-film model that matches the measured growth rates of the floes. For the replenishment flux (F_{spr}), we use the inferred pool resupply rate of ~1 ml/s (see section 5.1). For the $CaCO_3$ precipitation flux, we use the same formulation as in the thin-film model whereby there is a Ω (growth rate) dependence to the isotopic fractionation between $CaCO_3$ and CO_3^{2-} (Devriendt et al. 2017).

There are eight differential equations in the box model:

$$\frac{\partial[\mathrm{CO_2}]}{\partial t} = \{\text{reaction terms, Eq. 5}\} + \frac{F_{\mathrm{spr}}}{V_{\mathrm{pool}}}([\mathrm{CO_2}]_{\mathrm{spr}} - [\mathrm{CO_2}]) + \frac{F_{\mathrm{cr}}}{V_{\mathrm{pool}}}([\mathrm{CO_2}]_{\mathrm{cr}} - [\mathrm{CO_2}]) \qquad \text{Eq. 11}$$

$$\frac{\partial[\mathrm{EIC}]}{\partial t} = \{\text{reaction terms, Eq. 6}\} + \frac{J_{\mathrm{atm}} \cdot SA_{\mathrm{pool}}}{V_{\mathrm{pool}}} + \frac{F_{\mathrm{spr}}}{V_{\mathrm{pool}}}([\mathrm{EIC}]_{\mathrm{spr}} - [\mathrm{EIC}]) + \frac{F_{\mathrm{cr}}}{V_{\mathrm{pool}}}([\mathrm{EIC}]_{\mathrm{cr}} - [\mathrm{EIC}]) - J_{\mathrm{CaCO_3}} \cdot \mathrm{Sp} \qquad \text{Eq. 12}$$

$$\frac{\partial[\mathrm{Ca}^{2+}]}{\partial t} = \frac{F_{\mathrm{spr}}}{V_{\mathrm{pool}}}([\mathrm{Ca}^{2+}]_{\mathrm{spr}} - [\mathrm{Ca}^{2+}]) + \frac{F_{\mathrm{cr}}}{V_{\mathrm{pool}}}([\mathrm{Ca}^{2+}]_{\mathrm{cr}} - [\mathrm{Ca}^{2+}]) - J_{\mathrm{CaCO_3}} \cdot \mathrm{Sp} \qquad \text{Eq. 13}$$

$$\frac{\partial[\mathrm{Alk}]}{\partial t} = \frac{F_{\mathrm{spr}}}{V_{\mathrm{pool}}}([\mathrm{Alk}]_{\mathrm{spr}} - [\mathrm{Alk}]) + \frac{F_{\mathrm{cr}}}{V_{\mathrm{pool}}}([\mathrm{Alk}]_{\mathrm{cr}} - [\mathrm{Alk}]) - 2 \cdot J_{\mathrm{CaCO_3}} \cdot \mathrm{Sp} \qquad \text{Eq. 14}$$

$$\frac{\partial[^{13}\mathrm{CO_2}]}{\partial t} = \{\text{reaction terms, Eq. 9}\} + \frac{F_{\mathrm{spr}}}{V_{\mathrm{pool}}}(^{13}R_{\mathrm{CO_{2(spr)}}}[\mathrm{CO_2}]_{\mathrm{spr}} - [^{13}\mathrm{CO_2}]) + \frac{F_{\mathrm{cr}}}{V_{\mathrm{pool}}}(^{13}R_{\mathrm{CO_{2(cr)}}}[\mathrm{CO_2}]_{\mathrm{cr}} - [^{13}\mathrm{CO_2}]) \qquad \text{Eq. 15}$$

$$\frac{\partial[^{13}\mathrm{EIC}]}{\partial t} = \{\text{reaction terms, Eq. 10}\} + \frac{J_{\mathrm{atm}} \cdot SA_{\mathrm{pool}}}{V_{\mathrm{pool}}} \cdot (^{13}R_{\mathrm{EIC_{(hydrox)}}}) + \frac{F_{\mathrm{spr}}}{V_{\mathrm{pool}}}(^{13}R_{\mathrm{EIC_{(spr)}}}[\mathrm{EIC}]_{\mathrm{spr}} - [^{13}\mathrm{EIC}]) + \frac{F_{\mathrm{cr}}}{V_{\mathrm{pool}}}(^{13}R_{\mathrm{EIC_{(cr)}}}[\mathrm{EIC}]_{\mathrm{cr}} - [^{13}\mathrm{EIC}]) - J_{\mathrm{CaCO_3}} \cdot \mathrm{Sp} \cdot \frac{[^{13}\mathrm{EIC}]}{[\mathrm{EIC}]} \cdot (^{13}\alpha_{\mathrm{CaCO_3-EIC}}) \qquad \text{Eq. 16}$$

$$\frac{\partial[\mathrm{C^{18}OO}]}{\partial t} = \{\text{reaction terms, Eq. 11}\} + \frac{F_{\mathrm{spr}}}{V_{\mathrm{pool}}}(^{18}R_{\mathrm{CO_{2(spr)}}}[\mathrm{CO_2}]_{\mathrm{spr}} - [\mathrm{C^{18}OO}]) + \frac{F_{\mathrm{cr}}}{V_{\mathrm{pool}}}(^{18}R_{\mathrm{CO_{2(cr)}}}[\mathrm{CO_2}]_{\mathrm{cr}} - [\mathrm{C^{18}OO}]) \qquad \text{Eq. 17}$$

$$\frac{\partial[^{18}\mathrm{EIC}]}{\partial t} = \{\text{reaction terms, Eq. 12}\} + \frac{J_{\mathrm{atm}} \cdot SA_{\mathrm{pool}}}{V_{\mathrm{pool}}} \cdot (^{18}R_{\mathrm{EIC_{(hydrox)}}}) + \frac{F_{\mathrm{spr}}}{V_{\mathrm{pool}}}(^{18}R_{\mathrm{EIC_{(spr)}}}[\mathrm{EIC}]_{\mathrm{spr}} - [^{18}\mathrm{EIC}]) + \frac{F_{\mathrm{cr}}}{V_{\mathrm{pool}}}(^{18}R_{\mathrm{EIC_{(cr)}}}[\mathrm{EIC}]_{\mathrm{cr}} - [^{18}\mathrm{EIC}]) - J_{\mathrm{CaCO_3}} \cdot \mathrm{Sp} \cdot \frac{[^{18}\mathrm{EIC}]}{[\mathrm{EIC}]} \cdot (^{18}\alpha_{\mathrm{CaCO_3-EIC}}) \qquad \text{Eq. 18}$$

As a reference case, we use $SA_{pool} = 1$ m^2, Sp = 0.1 m^2/L and $V_{pool} = 100$L. This value of Sp is much smaller than the value used in the thin-film model because $V_{pool} >> V_{film}$ and there is a much higher surface area density of $CaCO_3$ in the thin film than in the bulk pool. The atmospheric DIC flux is $F^*_{atm} = 6 \times 10^{-7}$ mol/s, which is much greater than the spring DIC replenishment flux of $F^*_{spring} = F_{spring}[DIC]_{spring} = 3.5 \times 10^{-8}$ mol/s, implying that the isotopic results are not sensitive to the $\delta^{13}C$ of spring water because of its low DIC concentration. The spring flux still plays an important role, however, because it resupplies dissolved Ca^{2+} at a rate of 1.5×10^{-6} mol/s, which is comparable to the DIC flux from the atmosphere.

The results of running the model to steady state for different values of F^*_{creek} at constant F^*_{atm} and F^*_{spring} are displayed in Fig. 14. In each panel there are three curves corresponding to different initial pH values of the pool (Fig. 14a). The change in steady state pH, Ca^{2+}, and [DIC] occurs approximately where F^*_{creek} overtakes F^*_{atm} (Figs. 14a-c). The steady state Ω and surface area normalized growth rate can be tuned by adjusting SA_{pool}, Sp, and V_{pool} (Supplement), but since these parameters have a limited effect on the overall isotopic results, they will not be discussed further.

The isotopic results of the box model are displayed in Fig. 15. The light endmember of the array corresponds to low $F^*_{\text{creek}}/F^*_{\text{atm}}$. As the creek DIC flux increases, the pH decreases (shown by red circled numbers for the $pH_i = 12.0$ case) and the $\delta^{18}O$-$\delta^{13}C$ values move away from the kinetic limit and up the 1:1 line. Importantly, the pH remains above 11 for the entire part of the array below the equilibrium calcite line. The extreme heavy end of the array corresponds to high $F^*_{\text{creek}}/F^*_{\text{atm}}$ and steady state pH values below ~11. A key outcome of mixing of creek DIC to the high pH pool is that the oxygen isotopic composition of HCO_3^- can become isotopically distilled to higher-than-equilibrium values as it is converted to the isotopically lighter CO_3^{2-}. This can account for the cluster of carbonate samples exhibiting higher-than-equilibrium values. The extent of distillation is particularly sensitive to the initial pH, or more generally, the relative alkalinities of the spring versus creek water.

In Fig. 15, the CO_2 distillation trajectory illustrates what would occur if all incoming atmospheric CO_2 were to undergo hydroxylation without an opportunity for atmospheric equilibrium exchange. The isotopic data show no evidence to support this, indicating that CO_2 exchanges with, and is replenished by, the atmosphere faster than it is converted to HCO_3^- by hydroxylation. This result supports the local equilibrium assumption in the thin-film model and our treatment in the box model of CO_2 entering the bulk pool as EIC with an isotopic composition reflecting the kinetic limit of CO_2 hydroxylation. The DIC equilibration trajectory shows the isotopic behavior of the EIC as the ratio between HCO_3^- dehydroxylation and CO_2 hydroxylation increases from 0 to 1. The isotopic data show no evidence of partial equilibration, indicating that the HCO_3^- dehydroxylation rate is negligible relative to the CO_2 hydroxylation rate. This is supported by modeling results, which indicate that an unrealistic $V_{pool}/SA_{pool} > 1000$ is required in the model framework to yield an appreciable equilibration trajectory (Suppl. Fig. S12).

5.4 Potential paleoenvironmental applications

The samples from old (unknown age) laminated Ca-carbonate from BSC are shifted to the right of the array of modern Ca-carbonates (Fig. 8). A likely explanation is that they formed at a time when atmospheric CO_2 had a heavier, pre-industrial $\delta^{13}C$ value, as shown schematically in Fig. 8. This feature of the data suggests that the $\delta^{13}C$ of pre-industrial atmospheric CO_2 may be recoverable from ancient travertine, some of which is as old as 7000 years at The Cedars (^{14}C ages 950-7100 years, Table S4 in the Supplement).

The $\delta^{18}O$ values of old travertines and most modern travertines are close to the end-member $\delta^{18}O$ value reflecting HCO_3^- isotopically equilibrated with creek water (Beck et al., 2005). This suggests surface water DIC is the dominant carbon supply to travertine formation at The Cedars. Hence, old travertines $\delta^{18}O$ at The Cedars are expected to primarily reflect the oxygen isotope composition of past precipitation and creek water temperature.

5.5 Comparison to Oman carbonates

The $\delta^{13}C$-$\delta^{18}O$ array for the Oman carbonates (Fig. 1) is similar to that for The Cedars. The slopes are indistinguishable but there are two noteworthy differences. First, the lightest $\delta^{18}O$ value in the Oman array is about 2‰ heavier than at The Cedars despite atmospheric CO_2 having essentially the same isotopic composition in both places. The difference in light isotope limits thus appears to be a consequence of the $\delta^{18}O$ of H_2O and OH^- being about 6‰ higher in Oman, with OH^- contributing 1/3 of the oxygen to CO_3^{2-} during hydroxylation (Falk et al., 2016). Second, the Oman data is considerably more scattered at the heavy end of the array (Fig. 1). The fact that the data is more tightly clustered at the light end of the array makes sense because the isotopic composition of $CO_{2(atm)}$ does not vary by more than 1-2‰

worldwide (Trolier et al., 1996), and the hydroxylation KFF* only varies by 1.5‰ over the 21-32°C range (see section 5.3.2. above). The scatter at the heavy end of the array is most likely due to variable $\delta^{13}C$ of DIC in alkaline spring waters and other DIC sources over the large area (50 x 200 km) sampled (Falk et al., 2016). By contrast, The Cedars springs lie within a 0.5 km^2 area where the $\delta^{13}C$ of DIC is less variable, as evidenced by the tighter clustering of data at the heavy end of the array.

Conclusions

We investigated the textural and isotopic characteristics of carbonates that precipitate from ultrabasic (pH ~ 11-12) spring pools at The Cedars, California. The pools are fed by spring waters that have low [DIC], low Mg/Ca, and relatively high [Ca^{2+}] as a consequence of serpentinization and Mg-carbonate precipitation in the subsurface. Once the spring water reaches the surface, CO_2 from the atmosphere enters and a thin film of Ca-carbonate floe crystallizes and is held in place by surface tension. The initial polymorph to crystallize is aragonite, followed by calcite on the underside of the floe as it thickens. The preference of aragonite over calcite in this case is likely controlled by pH not by high Mg/Ca ratio or high supersaturation.

Calcium isotopic fractionation between Ca-carbonates and their host solution is sensitive to growth rate. The $\Delta^{44/40}Ca$ values retrieved from five carbonate-water pairs are indistinguishable, with an average value of -0.75±0.07‰ (±95% confid.). The Ca-carbonate growth rates are based on thickness measurements of surface floes of known age and are estimated to be the range of $4.8x10^{-7}$ mol/m^2/sec to $8.0x10^{-7}$ mol/m^2/sec. This value is in good agreement with the growth rate dependence of $\Delta^{44/40}Ca$ determined from laboratory experiments (Tang et al., 2008; Watkins et al., 2017) and modeling (DePaolo, 2011; Nielsen et al., 2012), allowing for differences in temperature and pH.

Ca-carbonates display an extreme range (>20‰) in carbon and oxygen isotope compositions. The $\delta^{13}C$ and $\delta^{18}O$ values co-vary along a 1:1 line which trends toward the isotopic composition of isotopically equilibrated DIC from surface waters and pointing toward atmospheric CO_2. Most of the samples are lighter in $\delta^{18}O$, some by as much as 15‰, than the expected equilibrium value at 17.4°C. The extreme light

HCO_3^-. The HCO_3^- rapidly deprotonates and is nearly quantitatively converted to CO_3^{2-} ions, which then reacts with Ca^{2+} to precipitate $CaCO_3$. We estimate the hydroxylation KFF's to be about -17‰ relative to $CO_{2(aq)}$ for carbon ($\delta^{13}C$) and -7‰ relative to '$CO_{2(aq)}$ + H_2O^-' for oxygen ($\delta^{18}O$). These compare favorably to other estimates based on analysis of natural samples, but discrepancies remain between field and laboratory studies.

We adapted the kinetic isotopic fractionation model from Chen et al. (2018) to further investigate mechanisms of Ca-carbonate precipitation and kinetic isotope fractionation. The DIC in solution evolves chemically and isotopically according to the reaction rate equations in the DIC-water-$CaCO_3$ system. Using known (or reasonably well constrained) isotope-specific reaction rate constants, along with values for the fluxes that are constrained from the literature and our own measurements, the model reproduces the 1:1 co-variation if (1) the residence time of DIC in solution is much shorter than the equilibration time; (2) CO_2 exchange with the atmosphere is efficient so that the incoming CO_2 does not become isotopically distilled when being converted to HCO_3^-; and (3) the isotopic composition of the isotopically equilibrated spring and creek waters also lies near the 1:1 line defined by the composition of atmospheric CO_2 and the isotopically lightest data points. The model can also match the observation that some of the carbonates are isotopically heavier than the equilibrium value, owing to isotopic distillation of HCO_3^- from creek water as it is nearly quantitatively converted to CO_3^{2-} during mixing with pool water.

Acknowledgements

We are grateful to Roger Raiche for access and transport to The Cedars and for guiding us to the various fascinating spring features at The Cedars. We thank Shaun T. Brown for his occasional assistance in the field, and for his advice on Ca isotopic measurement. We gratefully thank Peter Kelemen (Columbia Univ.) for providing the ^{14}C ages of travertine samples reported in the Supplement. This research was supported by the US Department of Energy, Office of Science, Office of Basic Energy Sciences under Award No. DE-AC02-05CH11231 to Lawrence Berkeley National Laboratory.

References

Adkins J. F., Boyle E. A., Curry W. B. and Lutringer A. (2003) Stable isotopes in deep-sea corals and a new mechanism for ‘‘vital effects’’. *Geochim. Cosmochim. Acta* **67**, 1129–1143.

Barkan, E. and Luz, B. (2012), High-precision measurements of $^{17}O/^{16}O$ and $^{18}O/^{16}O$ ratios in CO_2. *Rapid Commun. Mass Spectrom.* **26**, 2733-2738. doi:10.1002/rcm.6400

Barnes, I., LaMarche V. C. and Himmelberg G. (1967) Geochemical evidence of present-day serpentinization. *Science* **156**, 830-832.

Barnes, I. and O'Neil, J. (1969) The Relationship between Fluids in Some Fresh Alpine-Type Ultramafics and Possible Modern Serpentinization, Western United States. *Geol. Soc. of Amer. Bull.* **80**, 1947-1960.

Barnes, I., O'Neil, J. and Trescases, J. J. (1978) Present day serpentinization in New-Caledonia, Oman and Yugoslavia. *Goechim. Cosmochim. Acta* **42**, 144-145.

Beck, W. C., Grossman, E. L. and Morse, J. W. (2005) Experimental studies of oxygen isotope fractionation in the carbonic acid system at 15˚, 25˚, and 40˚C. *Geochim. Cosmochim. Acta* **69**, 3493-3503.

Blake, M. C., Jr., Graymer, R. W. and Stamski, R. E. (2002) Geologic map and map database of western Sonoma, northernmost Marin, and southernmost Mendocino Counties, California: U.S. Geological Survey Miscellaneous Field Studies Map MF-2402, version 1.0, scale 1:62,500.

Blake, M. C., Jr., Bailey, E. H. and Wentworth, C. M. (2012) The Cedars ultramafic mass, Sonoma County, California. U.S. Geological Survey Open-File Report, 2012-1164, 13p.

Böttcher, M. E., Neubert, N., Escher, P., von Allmen, K., Samankassou, E. and Nägler, T.F. (2018) Multi-isotope (Ba, C, O) partitioning during experimental carbonatization of a hyper-alkaline solution. *Chemie der Erde* **78**, 241-247.

Bottinga, Y. (1968) Calculation of fractionation factors for carbon and oxygen isotopic exchange in the system calcite-carbon dioxide-water. *J. Phys. Chem.* **72**, 800-808.

Chen, S., Gagnon, A. C. and Adkins, J. F. (2018) Carbonic anhydrase, coral calcification and a new model of stable isotope vital effects. *Geochim. Cosmochim. Acta* **236**, 179-197.

Choi, S. H., Shervais, J. W. and Mukasa, S. B. (2008) Supra-subduction and abyssal mantle peridotites of the Coast Range ophiolite, California. *Contrib. Mineral. Petrol.* **156**, 551-576.

Clark, I. D. and Fontes, J.–C. (1990) Palaeoclimatic reconstruction in northern Oman based on carbonates from hyperalkaline groundwaters. Quat. *Res.* **33**, 320-336.

Clark I. D. and Lauriol B. (1992) Kinetic enrichment of stable isotopes in cryogenic calcites. *Geochim. Cosmochim. Acta* **102**, 217–228.

Clark, I. D., Fontes, J.-C., Fritz, P. (1992) Stable isotope disequilibria in travertine from high pH waters: Laboratory investigations and field observations from Oman. *Contrib. Mineral. Petrol.* **56**, 2041-2050.

Coleman, R. G. (2000) Prospecting for ophiolites along the California continental margin. In *Ophiolites and Oceanic Crust: New Insights from Field Studies and the Ocean Drilling Program*. Dilek, Y. M., Moores, E. M., Elthon, D. and Nicolas, A., ed.s. Geological Society of American Special Paper 349, p.351-364.

Coplen, T. B. (2007) Calibration of the calcite-water oxygen-isotope geothermometer at Devils Hole, Nevada, a natural laboratory. *Geochim. Cosmochim. Acta* **71**, 3948-3957.

Craig, H., 1953. The geochemistry of the stable carbon isotopes. *Geochim. Cosmochim. Acta* **3**, 53-92.

Daëron, M.; Guo, W.; Eiler, J.; Genty, D.; Blamart, D.; Boch, R.; Drysdale, R.; Maire, R.; Wainer, K. and Zanchetta, G. (2011) (CO)-C-13-O-18 clumping in speleothems: Observations from natural caves and precipitation experiments. *Geochim. Cosmochim. Acta* **75**, 3303–3317.

Daëron, M.; Drysdale, R. N.; Peral, M.; Huyghe, D.; Blamart, D.; Coplen, T. B.; Lartaud, F. and Zanchetta, G. (2019) Most Earth-surface calcites precipitate out of isotopic equilibrium. Nature Comm. **10**, article 429 doi:10.1038/s41467-019-08336-5

DePaolo, D. J. (2011) Surface kinetic model for isotopic and trace element fractionation during precipitation of calcite from aqueous solutions. *Geochim. Cosmochim. Acta* **75**, 1039-1056.

Devriendt, L. S., Watkins, J. M. and McGregor, H. V. (2017) Oxygen isotope fractionation in the $CaCO_3$-DIC-H_2O system. *Geochim. Cosmochim. Acta* **214**, 115-142.

Dietzel M., Tang J., Leis A. and Köhler S. J. (2009) Oxygen isotopic fractionation during inorganic calcite precipitation – effects of temperature, precipitation rate and pH. *Chem. Geol.* **268**, 107–115.

DOE (1994) Handbook of methods for the analysis of the various parameters of the carbon dioxide system in seawater; version 2. ORNL/CDIAC.

Falk, E. S., Guo, W., Paukert, A. N., Matter, J. M., Mervine E. M. and Kelemen, P. B. (2016) Controls on the stable isotope compositions of travertine from hyperalkaline springs in Oman: Insights from clumped isotope measurements. *Geochim. Cosmochim. Acta* **192**, 1-28.

Guo, W. (2019) Kinetic clumped isotope fractionation in the DIC-H_2O-CO_2 system: patterns, controls and implication. *Geochim. Cosmochim. Acta* **268**, **230-257.**

Harms, P.A. (2015) Distribution of Tritium in Precipitation and Surface Water in California. MS Thesis, Calif. State Univ. East Bay

Hermoso, M.; Horner, T. J.; Minoletti, F. and Rickaby, R. E. M. (2014) Constraints on the vital effect in coccolithophore and dinoflagellate calcite by oxygen isotopic modification of seawater. *Geochim. Cosmochim. Acta* **141**, 612-627

Hu, Y.-B., Wolthers, M., Wolf-Gladrow, D. A. and Nehrke, G. (2015) Effect of pH and phosphate on calcium carbonate polymorphs precipitated at near-freezing temperature. *Crystl. Grwth. Design* **15**, 1596-1601.

Huang, S., Farkas, J. and Jacobsen, S. B. (2010) Calcium isotopic fractionation between clinopyroxene and orthopyroxene from mantle peridotites. *Earth Planet. Sci. Lttrs.* **292**, 337-344.

Jones, B. (2017) Review of calcium carbonate polymorph precipitation in spring systems. *Sed. Geol.* **353**, 64-75.

Kawano, J., Shimobayashi, N., Miyake, A. and Kitamura, M. (2009) Precipitation diagram of calcium carbonate polymorphs: its construction and significance. *J. Phys.: Condens. Matter* **21**, doi:10.1088/0953-8984/21/42425102

Keeling, C. D., Piper, S. C., Bacastow, R. B., Wahlen, M., Whorf, T. P., Heimann, M. and Meijer, H. A. (2001) Exchanges of atmospheric CO_2 and $^{13}CO_2$ with the terrestrial biosphere and oceans from 1978 to 2000. I. Global aspects, SIO Reference Series, No. 01-06, Scripps Institution of Oceanography, San Diego, 88 pages.

Kelemen, P.B., Matter, J., Streit, E.E., Rudge, J.F., Curry, W.B. and Blusztajn, J. (2011) Rates and mechanisms of mineral carbonation in peridotite: natural processes and recipes for enhanced, in situ CO_2 capture and storage. *Annual Review of Earth and Planetary Sciences*, **39**, 545-576.

Kim S.-T., Hillaire-Marcel C. and Mucci A. (2006) Mechanisms of equilibrium and kinetic oxygen isotope effects in synthetic aragonite at 25 ˚C. *Geochim. Cosmochim. Acta* **70**, 5790–5801.

Kim S.-T., O'Neil J. R., Hillaire-Marcel C. and Mucci A. (2007) Oxygen isotope fractionation between synthetic aragonite and water: influence of temperature and Mg2+ concentration. *Geochim. Cosmochim. Acta* **71**, 4704–4715.

Kimball, J. B.; Dunbar R. B. and Guilderson, T. P. (2014) Oxygen and carbon isotope fractionation in calcitic deep-sea corals: Implications for paleotemperature reconstructions. *Chem. Geol.* **381**, 223–233.

Leleu, T., Chavagnac, V., Delacour, A., Noiriel, C., Ceuleneer, G., Aretz, M., Rommevaux, C. and Ventalon, S. (2016) Travertine associated with hyperalkaline springs: evaluation as a proxy for paleoenvironmental conditions and sequestration of atmospheric CO$_2$. *J. Sed. Res.* **86**, 1328-1343.

Lian, B., Hu, Q., Chen, J., Ji, J. and Teng, H. H. (2006) Carbonate biomineralization induced by soil bacterium Bacillus megaterium. *Geochim. Cosmochim. Acta* **70**, 5522-5535.

Matsumoto, M., Fukunaga, T., and Onoe, K. (2010) Polymorph control of calcium carbonate by reactive crystallization using a microbubble technique. *Chem. Eng. Res. Design* **88**, 1624-1630.

McConnaughey, T. (1989) ^{13}C and ^{18}O isotopic disequilibrium in biological carbonates: I. Patterns. *Geochim. Cosmochim. Acta* **53**, 151-162.

Meister, P., Johnson, O., Coresetti, F. and Nealson, K. H. (2011) Magnesium inhibition controls spherical carbonate precipitation in ultrabasic springwater (Cedars, California) and culture experiments. In *Advances in Stromatolite Goebiology*, Lecture Notes in Earth Sciences 131, doi: 10.1007/978-3-642-10415-2_6

Mervine, E. M., Humphris, S. E., Sims, K. W., Kelemen, P. B. and Jenkins, W. J. (2014) Carbonation rates of peridotite in the Samail Ophiolite, Sultanate of Oman, constrained through ^{14}C dating and stable isotopes. *Geochim. Cosmochim. Acta* **126,** 371-397.

Millero, F. J., Graham, T. B., Huang, F., Bustos-Serrano, H. and Pierrot, D. (2006) Dissociation constants of carbonic acid in seawater as a function of salinity and temperature. *Marine Chemistry,* **100**, 80-94.

Mook, W. (1986) ^{13}C in atmospheric CO$_2$. *Netherlands Journal of Sea Research* **20**, 211-223.

Morrill, P. L., Kuenen, J. G., Johnson, O. J., Suzuki, S., Rietze, A., Sessions, A. L., Fogel, M. L. and Nealson, K. H. (2013) Geochemistry and geobiology of a pesent-day serpentinization site in California: The Cedars. *Goechim. Cosmochim. Acta* **109**, 222-240.

Nielsen, L. C., Druhan, J. L., Yang, W., Brown, S. T. and DePaolo, D. J. (2011). Calcium Isotopes as Tracers of Biogeochemical Processes. In M. Baskaran (Ed.), *Handbook of Environmental Isotope Geochemistry* (pp. 105–124). Berlin, Heidelberg: Springer Berlin Heidelberg. http://doi.org/10.1007/978-3-642-10637-8_7

Nielsen, L. C., DePaolo, D. J. and De Yoreo, J. J. (2012) Self-consistent ion-by-ion growth model for kinetic isotopic fractionation during calcite precipitation. *Geochim. Cosmochim. Acta* **86**, 166-181.

Nielsen, L. C., De Yoreo, J. J. and DePaolo, D. J. (2013) General model for calcite growth kinetics in the presence of impurity ions. *Geochim. Cosmochim. Acta* **115**, 200-114.

O’Neil, J. R. and Barnes, I. (1971) C13 and O18 compositions in some fresh-water carbonates associated with ultramafic rocks and serpentinites: western United States. *Geochim. Cosmochim. Acta* **35**, 687-697.

Pinsent, B. R. W., Pearson, L., Roughton, F. J. W. (1956) The kinetics of combination of carbon dioxide with hydroxide ions. *Trans. Faraday Soc.*, **52(11)**, 1512-1520.

Romanek, C. S., Grossman, E .L. and Morse, J. W. (1992) Carbon isotopic fractionation in synthetic aragonite and calcite: effects of temperature and precipitation rate. *Geochim. Cosmochim. Acta*, ***56***(1), 419-430.

Romanek, C. S., Morse, J. W. and Grossman, E. L. (2011) Aragonite kinetics in dilute solutions. *Aquatic Geochemistry* **17**, 339-356.

Sade, Z. and Halevy, I. (2017) New constraints on kinetic isotope effects during CO_2(aq) hydration and hydroxylation: Revisiting theoretical and experimental data. *Geochim. Cosmochim. Acta* **214**, 246-265

Sade, Z. and Halevy, I. (2018) Corrigendum to "New constraints on kinetic isotope effects during CO_2(aq) hydration and hydroxylation: Revisiting theoretical and experimental data" [Geochim. Cosmochim. Acta 214 (2017) 246-265]. *Geochim. Cosmochim. Acta*, **225**, 237-240.

Spero, H. J.; Bijma, J.; Lea, D. W. and Bemis, B. E. (1997) Effect of seawater carbonate concentration on foraminiferal carbon and oxygen isotopes. *Nature* **390**, 497-500.

Sun, W., Jayaraman, S., Chen, W., Persson. K A. and Ceder, G. (2015) Nucleation of metastable aragonite $CaCO_3$ in seawater. *Proc.s Natl. Acad. Sci.s* **112**, 3199-3204.

Suzuki, S., Ishii, S., Wu, A., Cheung, A., Tenney, A., Wanger, G., J Gijs Kuenen, J. G., Nealson, K. H. (2013) Microbial diversity in The Cedars, an ultrabasic, ultrareducing, and low salinity serpentinizing ecosystem. *Proc.s Natl. Acad. Sci.s*, **110(30)**, 15336-15341.

Suzuki, S., Ishii, S., Hoshino, T., Rietze, A., Tenney, A., Morrill, P.L., Inagaki, F., Kuenen, J. G. and Nealson, K. H. (2017) Unusual metabolic diversity of hyperalkaliphilic microbial communities associated with subterranean serpentinization at The Cedars. *The ISME Journal* **11**, 2584-2598.

Tai, C. Y. and Chen, F. B. (1998) Polymorphism of $CaCO_3$ precipitated in a constant-composition environment. *AIChE Journal* **44**, 1790-1798.

Talbot M. R. (1990) A review of the palaeohydrological interpretation of carbon and oxygen isotopic ratios in primary lacustrine carbonates. *Chem. Geol.* **80**, 261-279.

Tang J., Dietzel M., Böhm F., Kohler S. and Eisenhauer A. (2008) Sr^{2+}/Ca^{2+} and $^{44}Ca/^{40}Ca$ fractionation during inorganic calcite formation: II. Ca isotopes. *Geochim. Cosmochim. Acta* **72**, 3733–3745.

Tourney, J. and Ngwenya, B. T. (2009) Bacterial extracellular polymeric substances (EPS) mediate CaCO3 morphology and polymorphism. *Chem. Geol.* **202**, 138-146.

Tremaine, D. M.; Froelich, P. N. and Wang Y. (2011) Speleothem calcite farmed *in situ*: Modern calibration of $\delta^{18}O$ and $\delta^{13}C$ paleoclimate proxies in a continuously-monitored natural cave system. *Geochim. Cosmochim. Acta* **75**, 4929–4950.

Trolier, M.; White, J. W. C.; Tans, P. P.; Masarie, K. A. and P. A. Gemery (1996) Monitoring the isotopic composition of atmospheric CO_2: Measurements from the NOAA Global Air Sampling Network. *J. Geophys. Res.* **101**, 25,897– 25,916, 1996.

Uchikawa, J. and Zeebe, R. E. (2012) The effect of carbonic anhydrase on the kinetics and equilibrium of the oxygen isotope exchange in the CO_2-H_2O system: Implications for ^{18}O vital effects in biogenic carbonates. *Geochim. Cosmochim. Acta* **95**, 15-34.

Usdowski, E. and Hoefs, J. (1986) $^{13}C/^{12}C$ partitioning and kinetics of CO_2 adsorption by hydroxide buffer solutions. *Earth Planet. Sci. Lttrs.* **80**, 130-134.

Usdowski E., Michaelis J., Böttcher M. E. and Hoefs J. (1991) Factors for the oxygen isotope equilibrium fractionation between aqueous and gaseous CO2, carbonic acid, bicarbonate, carbonate, and water (19 ˚C). *Z. Phys. Chem.* **170**, 237–249.

Usdowski E. and Hoefs J. (1993) Oxygen isotope exchange between carbonic acid, bicarbonate, carbonate, and water: A re-examination of the data of McCrea (1950) and an expression for the overall partitioning of oxygen isotopes between the carbonate species and water. *Geochim. Cosmochim. Acta* **57**, 3815–3818.

Vogel, J., Grootes, P. and Mook, W. (1970) Isotopic fractionation between gaseous and dissolved carbon dioxide. *Zeitschrift für Physik* **230**, 225-238.

Watkins, J. M., Nielsen, L. C., Ryerson, F. J. and DePaolo, D. J. (2013) The influence of kinetics on the oxygen isotope composition of calcium carbonate. *Earth Planet. Sci. Lttrs.* **375**, 349-360.

Watkins J. M., Hunt J. D., Ryerson F. J. and DePaolo D. J. (2014) The influence of temperature, pH, and growth rate on the 18O composition of inorganically precipitated calcite. *Earth Planet. Sci. Lett.* **404**, 332–343.

Watkins, J. M., DePaolo, D. J. and Watson, E. B., 2017. Kinetic fractionation of non-traditional stable isotopes by diffusion and crystal growth reactions. *Reviews in Mineralogy and Geochemistry*, *82*(1), pp.85-125.

White, J. W. C., Vaughn, B. H. and Michel S. E. (2015) University of Colorado, Institute of Arctic and Alpine Research (INSTAAR), Stable Isotopic Composition of Atmospheric Carbon Dioxide (^{13}C and ^{18}O) from the NOAA ESRL Carbon Cycle Cooperative Global Air Sampling Network, 1990-2014, Version: 2015-10-26.

Wolthers, M., Nehrke, G., Gustafsson, J. P. and Van Cappellen, P. (2012) Calcite growth kinetics: Modeling the effect of solution stoichiometry. *Geochim. Cosomochim. Acta* **77(15)**, 121-134.

Yan, H., Schmitt, A.-D., Liu, Z., Gangloff, S., Sun, H., Chen, J.; and Chabaux, F. (2016) Calcium isotopic fractionation during travertine deposition under different hydrodynamic conditions: Examples from Baishuitai (Yunan, SW China). *Chem. Geol.* **426**, 60-70.

Yumol, L. M., Uchikawa, J. and Zeebe, R. E. (2020). Kinetic isotope effects during CO2 hydration: Experimental results for carbon and oxygen fractionation. *Geochimica et Cosmochimica Acta* **279**, 189-203.

Žák, K.; Onac, B. P. and Perşoiu, A., (2008) Cryogenic carbonates in cave environments: A review. *Quaternary International*, **187(1)**, 84-96.

Zeebe, R.E., 2011. On the molecular diffusion coefficients of dissolved CO_2, HCO_3^-, and CO_3^{2-} and their dependence on isotopic mass. *Geochimica et Cosmochimica Acta*, *75*(9), pp.2483-2498.

Zeebe, R. E. (2014) Kinetic fractionation of carbon and oxygen isotopes during hydration of carbon dioxide. *Geochim. Cosmochim. Acta* **139**, 540-552.

Zeebe, R.E., 2020. Oxygen isotope fractionation between water and the aqueous hydroxide ion. *Geochimica et Cosmochimica Act* **289**, 182-195.

Zeebe, R.E.; Wolf-Gladrow, D.A. (2001) CO_2 in seawater: equilibrium, kinetics, isotopes. Elsevier Oceanography Series, Vol. 65. Elsevier, Amsterdam. 360p

Figure Captions

Figure 1. Plot of $\delta^{13}C$ vs. $\delta^{18}O$ of carbonates associated with high pH springs in Oman emanating from ultramafic rocks of the Samail ophiolite. The dashed box represents the expected range of equilibrium values of $\delta^{13}C$ and $\delta^{18}O$ of DIC from Falk et al. (2016). The data were compiled from Falk et al. (2016), Mervine et al. (2014), Clark et al. (1992) and Clark and Fontes (1990). The solid grey line represents a 1 to 1 relationship between $\delta^{13}C$ and $\delta^{18}O$.

Figure 2. Maps showing the location of The Cedars, the local geology, and sampling locations (modified after Morrill et al. 2013). Using the nomenclature of Morrill et al. (2013) BSC=Barnes Spring Complex, GPS=Grotto Pool Springs. The Wedding Cake is at the NS1 locality above Mineral Falls.

Figure 3. Photos of a spring pool adjacent to Austin Creek at the Barnes Spring Complex (BSC) taken in October, 2018. The left panel shows examples of Ca-carbonate floe at the pool surface (much floe has been cleared away in sample collection, giving a view of the pool bottom), Ca-carbonate snow at the bottom of the pool, the Ca-carbonate rim of the pool where water exits the pool, and old travertine deposits. The dark outcrops are ultramafic rocks of The Cedars. The right panel shows a closer view from a different angle of the pool featured in the left panel.

Figure 4. SEM images of floe Ca-carbonate from BSC pool surface. **(A)** Image of the inferred top-side of the floe (Carb D). Texture consists of radiating crystals of aragonite (identified in XRPD) in a horizontal plane (detail in inset 1), showing in places a plumose/branching texture (inset 2). Over all the surface of this side is relatively flat. (**B)** The inferred bottom-side of the floe. To right is an enlargement of the area in the dashed box in the left panel. Left image show calcite rhombs sitting on sprays of aragonite crystals. In contrast to the side shown in A, this side is hummocky and less smooth. In this example, there are open areas between aragonite sprays representing approximately 10-15% of the area of the floe. **(C)** SEM image comparing the top and bottom sides of an another example of floe carbonate (flakes were placed next to each other in opposite orientations) from the Barnes Complex. In this case the material was collected to preserve the original orientation of the sample. The top side is relatively smooth showing horizontal sprays of aragonite crystals, while the bottom side (the side facing down into the water) shows downward orientated sprays of aragonite crystals with scattered rhombs of calcite.

Figure 5. SEM images showing cross sections of BSC floe material representing approximately eight days of growth and (inset) four days of growth. The top side is to the left, and the bottom side (facing down into the pool water) to the right. The 8-day image indicates a thickness of 20-25 microns, with about half that thickness after four days growth, suggesting a constant growth rate of ~3 microns/day.

Figure 6. The pH vs. Mg/Ca molar ratio for samples of Austin Creek, and creek/spring mixtures. Samples with pH ≤ 11 are shown as red circles. Curves model mixing between BSC Spring water with pH=11.8, and Mg/Ca molar ratio of 0.002 with Austin Ck water taken upstream of the BSC in April at high-flow (upper,

grey curve) and in August near low-flow (lower, black curve). Dashed line for a Mg/Ca ratio of 2.

Figure 7. (A) An ln-ln Rayleigh fractionation model plot for high-pH waters (>11.0) from The Cedars springs and pools. The value of F (the fraction of Ca remaining) is based on the water sample with the highest Ca concentration (58 ppm) and lowest δ^{44}Ca (0.02±0.06) from the seep above the Wedding Cake Pool (sample F9). The slope of the best-fit line gives a fractionation of -0.76±0.12‰ (95% confid.). **(B)** Summary of the calcium isotope fractionation factors (Δ^{44}Ca) determined from carbonate-water pairs (red circles) and the Rayleigh model shown in A for waters with pH ≥11.0. Uncertainties shown at ±95% confidence.

Figure 8. The carbon and oxygen isotopic compositions of Ca-carbonate samples from The Cedars. Open circles shows data from Meister et al. 2011. Vertical arrows along the x-axis show the δ^{13}C of total inorganic C (TIC) from pool sample at the BSC, and TIC for a sample of Austin Creek (Morrill et al. 2013). Shown for reference is the isotopic composition of atmospheric CO_2 (Pt Arena, CA data from White et al. (2015)) and an estimate for pre-industrial atmospheric CO_2. The black line shows the slope of a 1 to 1 correlation between δ^{18}O and δ^{13}C, and is parallel to the blue dashed line provided for visual reference.

Figure 9. A comparison between field observations at The Cedars to experimental data at 25 ˚C from Tang et al. (2008) (white circles), experimental data at 25 ˚C and 15 ˚C from Watkins et al. (2017) (red and blue circles respectively), and to data for field experiments involving Ca-carbonate (calcite only) growth on plexiglass slides from Yan et al. 2016. The solid blue curve is Model 1 from DePaolo (2011).

Figure 10. Conceptual model for the evolution of Ca-carbonate floes at the surface of high pH waters. Within the water surface layer (not shown to scale) aragonite nucleation/growth rates are greater than those of calcite, consistent with ~pH=11 (Tai and Chen 1998). As the aragonite layer thickens down into the water below with pH ≥11.5 calcite nucleation/growth rates become greater than aragonite (Tai and Chen 1998) resulting in overgrowth by calcite rhombs. Through disturbance of the pool's surface due to wind, falling debris, rain, etc. the surface tension is broken and the floe sinks to the bottom where continued calcite precipitation can occur. With the surface cleared, the process of floe formation begins again.

Figure 11. Schematic diagram showing how the two stages of the quantitative model fit together. The thin-film model focuses on processes within the 100 μm diffusional boundary layer at the pool-atmosphere interface and tracks spatial variations in DIC species' concentrations and isotopic compositions. The box model focuses on the larger scale of the bulk pools and how the DIC species' concentrations and isotopic compositions vary as a function of three fluxes: (1) DIC from the thin film, (2) DIC replenishment from the spring water inflow and outflow, and (3) $CaCO_3$ precipitation.

Figure 12. Results of the thin-film model. Curves represent steady state profiles for different values of Sp. **(a)-(k)** Dissolved CO_2 is assumed to be in local chemical and isotopic equilibrium with the atmosphere at z = 0. As CO_2 diffuses downward, it

reacts with OH- to form isotopically light EIC, resulting in residual CO_2 that is isotopically heavy. The increase in DIC near the surface increases the supersaturation while decreasing the pH. Precipitation of $CaCO_3$ decreases $[Ca^{2+}]$ and EIC near the surface. **(I)** The light isotope limits of EIC and $CaCO_3$ are determined by the KFFs for hydroxylation and the proportion of CO_3^{2-} that gets converted to $CaCO_3$. A large Sp implies near complete conversion with concomitant isotopic distillation of CO_3^{2-} to values lighter than given by the KFF. In this case, the $CaCO_3$ records the isotopic composition of hydroxylated HCO_3^-.

Figure 13. Compilation of hydroxylation KFF's. **(A)** The carbon KFF is likely between -13 and -17‰. **(B)** The oxygen KFF is close to 0, meaning that the isotopic composition of HCO_3^- that forms by hydroxylation is indistinguishable from the composition of the weighted sum of reactants (CO_2+OH^-). **(C)** The oxygen KFF* is -6.8 ±0.8 when expressed relative to 'CO_2+H_2O'.

Figure 14. Box model results for pools of high pH water at The Cedars. **(a)-(f)** Steady state composition of the pool as a function of F^*_{creek} at fixed F^*_{spring} and F^*_{atm}.

Figure 15. Box model results for pools of high pH water at The Cedars using the same parameters as in Fig. 14. The carbon and oxygen isotopic composition of $CaCO_3$ (red curves) is heavier than the EIC (blue curve) due to partial equilibration between EIC and $CaCO_3$. The circles with red numbers represent the pH values along the pH_{ini} = 12 curve and show that pH remains high along the full array. Higher-than-equilibrium calcite forms when HCO_3^- from the creek gets isotopically distilled during conversion to CO_3^{2-}, which is then inherited by the $CaCO_3$. The green arrows show the trajectories of DIC equilibration and CO_2 distillation (all incoming CO_2 converted to HCO_3^-).

Tables 1-7 are below

Table 1. XRD results for mineral compositions of carbonate samples

Label	Description	Aragonite, %	Calcite, %	Vaterite, %	Hydromagnesite, %	Nitromagnesite, %	Brucite, %	Nesquehonite, %
Carb A	Wedding Cake rim	99.7±0.4	0.27±0.06	n.d.	n.d.	n.d.	n.d.	n.d.
Carb B	New Pool Xtl String	99.7±0.4	0.29±0.05	n.d.	n.d.	n.d.	n.d.	n.d.
Carb H	Floe GPS1	17.8±0.3	82.2±0.5	n.d.	n.d.	n.d.	n.d.	n.d.
Carb I	Floe BSC	21.7±0.6	77.8±0.9	0.5±0.2	n.d.	n.d.	n.d.	n.d.
Carb J	GPS filtered snow (pool 1)	68±0.5	0.14±0.06	n.d.	27.4±0.8	4.5±0.4	n.d.	n.d.
Carb K	GPS filtered snow (pool 2)	25.0±0.2	19.8±0.2	n.d.	49.5±0.5	2.3±0.2	0.5±0.08	3.0±0.1
Carb AA	Mixed spr/ck water at BSC	91.0±0.4	1.30±0.08	n.d.	n.d.	n.d.	7.7±0.4	n.d.
BSC	Floe from pool A, BSC. Powder	91.5±0.2	8.51±0.09	n.d.	n.d.	n.d.	n.d.	n.d.
BSC	Floe from pool A, BSC. Sheet	55.2±0.5	45±3	n.d.	n.d.	n.d.	n.d.	n.d.
PB-C1	Pool B snow, from bottom	86.0±0.8	7.1±0.2	n.d.	n.d.	n.d.	6.8±0.2	n.d.
PB-C2 bulk	Edge pool B, BSC. Whole sample	91.1±0.7	0.53±0.04	n.d.	n.d.	n.d.	8.4±0.6	n.d.
PB-C2 crust	Edge pool B, BSC. Outer surface	46.2±0.2	48.8±0.8	n.d.	n.d.	n.d.	5.0±0.2	n.d.
PE-C2 bulk	Edge pool E, BSC. Whole sample	91.0±0.6	5.9±0.1	n.d.	n.d.	n.d.	3.1±0.09	n.d.
PE-C2 crust	Edge pool E, BSC. Outer surface	77.5±0.4	17.9±0.09	0.6±0.2	n.d.	n.d.	4.1±0.2	n.d.

Table 2. Ca isotopic and chemical compositions of waters from The Cedars.

Label	Location	$\delta^{44}Ca_{BSE}$, ‰	±2σ	Ca, ppm*	K, ppm	Mg, ppm	Na, ppm	Sr, ppb	Mg/Ca molar	pH
F1	GPS pool under floe	0.26	0.16	34.9	6.98	0.07	342	1.41	0.0031	12.0
F2	BC spring	0.18	0.12	51.7	1.22	0.07	49	5.23	0.0020	11.8
F3	Wedding Cake Pool	1.23	0.06	12.2	0.54	34.8	14	0.79	4.53	11.3
F4	BC1 pool under floe	0.16	0.06	51.1	1.36	0.11	50	3.16	0.0033	11.5
F5	Ck inflow to New Pool	0.46	0.12	2.2	0.07	40.8	1.7	1.85	29.9	9.0
F6	New Pool next ppt.s	0.32	0.25	9.5	0.26	31.2	7.0	1.85	5.40	9.9
F7	GPS Upper filtrate	0.83	0.20	17.1	5.88	0.06	306	1.71	0.0057	12.1
F8	GPS spring	0.14	0.07	37.5	6.96	0.07	345	1.60	0.0026	12.1
F9	Wedding Cake seep	0.02	0.06	58.1	0.52	0.35	136	0.97	0.0099	11.4
F10	Pool G	0.50	0.26	39.3	1.27	0.19	57	3.0	0.0081	11.6
F11	Pool C	0.24	0.14	41.8	1.26	0.20	56	3.1	0.0079	11.6
F12	Blue Pool	0.12	0.07	51.0	1.27	0.18	57	3.3	0.0057	11.65
F13	BSC2 10/16	0.16	0.12	54.0	1.26	0.098	56	3.5	0.0030	11.7
F14	Pool E	0.27	0.21	41.7	1.57	0.198	57	3.1	0.0078	11.6
F15	Wedding Cake 9/16	0.14	0.11	47.8	0.76	9.8	20	3.5	0.338	11.3
4/14	Creek above Barnes Cpx			1.2†	0.06	49.0	1.6	1.37	66.0	7.8
8/16	Creek above Barnes Cpx			3.1†	0.10	40.9	4.0	1.83	21.8	8.7
8/13	Creek below Camp			8.0†	0.67	41.1	39	2.17	8.52	9.5

*Ca concentrations by isotope dilution except those marked † that were conducted by Q-ICPMS. Other element concentrations by Q-ICPMS, pH measured in the field.

Table 3. Ca, C, and O isotopic compositions of Ca-carbonates

Label	**Description**	$\delta^{44}\mathrm{Ca}_{\mathrm{BSE}}$, ‰	±2σ	$\delta^{13}\mathrm{C}_{\mathrm{VPDB}}$, ‰	$\delta^{18}\mathrm{O}_{\mathrm{VPDB}}$, ‰
Carb A	Wedding Cake rim (4/5/14)	-0.46	0.09	-14.62	-4.24
Carb B	New Pool xtl strings #1 (10/11/14)	-0.17	0.07	-11.78	-3.76
Carb C	New Pool encrustation (10/11/14)	-0.46	0.10	-12.00	-3.65
Carb D	BSC floe, upstream (10/11/14)	-0.77	0.11	-26.48	-19.06
Carb E	BSC floe, middle (10/11/14)	-0.69	0.08	-26.73	-18.32
Carb F	BSC floe, downstream (10/11/14)	-0.52	0.19	-26.66	-18.79
Carb G	New Pool xtl strings #2 (10/11/14)	-0.42	0.11	-12.34	-4.80
Carb H	GPS floe (10/11/14)	-0.38	0.02	-21.39	-13.47
Carb I	BSC large floe sample (10/11/14)	-0.66	0.06	-26.71	-18.71
Carb J	GPS upper filtered carb (10/11/14)	-0.68	0.04	-13.48	-0.36
Carb K	GPS filtered carb (10/11/14)	-0.65	0.07	-13.54	-5.13
Carb L	GPS floe (8/3/13)	-0.41	0.10	-23.04	-14.74
Carb M	Wedding Cake 1cm below rim (10/11/14)	--	--	-14.29	-3.56
Carb N	Wedding Cake 15cm below rim (10/11/14)	--	--	-15.08	-4.58
Carb P	Pool E floe (PE-C1) (10/7/16)	-0.48	0.07	-27.55	-19.58
Carb Q	Wedding Cake Floe (9/2/16)	-0.58	0.11	-17.45	-6.69
Carb R	BSC2 Floe (10/7/16)	-0.52	0.07	-25.50	-18.77

Table 4. Calculated values of Ca isotopic fractionation due to Ca-carbonate precipitation using data from Tables 2 and 3 for floe/water pairs

Observation	$\Delta^{44/40}\mathrm{Ca}$, ‰, ±2s
Rayleigh model with all high pH waters	-0.76±0.12
Wedding Cake (CarbQ – F15)	-0.72±0.16
BSC1 (Ave. of Carbs D,E,F, & I minus F4)	-0.84±0.11
BSC2 (Carb R-F13)	-0.68±0.14
BSC Pool E (CarbP-F14)	-0.75±0.22
GPS1 (CarbL-F1)	-0.67±0.19
Weighted Average Carb-Water	-0.75±0.07
Weighted Average all values	-0.75±0.06

Table 5. Compilation of equilibrium fractionation factors (EFFs; T in Kelvin unless otherwise noted)

Compounds	Equation	α (17.4°C)	Reference
Carbon isotopes			
$CO_2(g) - HCO_3^-$	$-9.483T^{-1} + 1.02389$	0.9913	Mook (1986)
$CO_2(aq) - HCO_3^-$	$-9.866T^{-1} + 1.02412$	0.9902	Mook (1986)
$CO_3^{2-} - HCO_3^-$	$-0.867T^{-1} + 1.00252$	0.9995	Mook (1986)
$CO_2(g) -$ Calcite	$\exp\left\{\frac{-2.4612 + \frac{7666.3}{T} - \frac{2988000}{T^2}}{1000}\right\}$	0.9886	Bottinga (1968)
Oxygen isotopes			
$CO_2(aq) - H_2O$	$\exp(2520T^{-2}+0.01212)$	1.0427	Beck et al. (2005)
$HCO_3^- - H_2O$	$\exp(2590T^{-2}-0.00189)$	1.0331	Beck et al. (2005)
$CO_3^{2-} - H_2O$	$\exp(2390T^{-2}-0.00270)$	1.0259	Beck et al. (2005)
Calcite $- H_2O$	$\exp\left(\frac{\frac{17747}{T} - 29.777}{1000}\right)$	1.0318	Coplen (2007), Watkins et al. (2013)
$OH^- - H_2O$	$1/[23.5-0.0728(T_C-25)]$ or	0.9765	Zeebe (2020)
$OH^- - H_2O$	$1/[19.1-0.0455(T_C-25)]$	0.9787	Zeebe (2020)

Table 6. Constants and parameters used in the model

Symbol	Meaning	Value	Reference/Note
Part I: Model parameters			
F_{spr}	Spring mass flux	0.001 kg-sol/s	To maintain [Ca^{2+}], see text
$[\text{DIC}]_{\text{spr}}$	Spring [DIC]	0.035 mM	Morrill et al. (2013)
$[Ca^{2+}]_{\text{spr}}$	Spring [Ca^{2+}]	1.3 mM	Morrill et al. (2013)
$[\text{Alk}]_{\text{spr}}$	Spring total alkalinity	2.6 mM	Calc. from DIC & pH
$[CO_2]_{\text{spr}}$	Spring $[CO_2]_{(aq)}$	$1.0\text{x}10^{-8}$ mM	Calc. from DIC & pH
$[\text{EIC}]_{\text{spr}}$	Spring $[HCO_3^-]+[CO_3^{2-}]$	0.035 mM	Calc. from DIC & pH
F_{cr}	Creek mass flux	Variable (kg-soln/s)	-
$[\text{DIC}]_{\text{cr}}$	Creek [DIC]	2.9 mM	Morrill et al. (2013)
$[Ca^{2+}]_{\text{cr}}$	Creek [Ca^{2+}]	0.13 mM	Morrill et al. (2013)
$[\text{Alk}]_{\text{cr}}$	Creek total alkalinity	3.0 mM	Calc. from DIC & pH
$[CO_2]_{\text{cr}}$	Creek $[CO_2]_{(aq)}$	0.011 mM	Calc. from DIC & pH
$[\text{EIC}]_{\text{cr}}$	Creek $[HCO_3^-]+[CO_3^{2-}]$	2.89 mM	Calc. from DIC & pH
J_{atm}	EIC flux through thin water film	$6\text{x}10^{-7}$ moles/m^2/s	Usdowski & Hoefs (1986)
SA_{pool}	Surface area of pool	1 m^2	-
J_{CaCO3}	Carbonate precipitation rate (moles/m^2/s)	$J_{\text{CaCO3}} = k_{\text{rate}}(\Omega-1)^{1.7}$	Romanek et al. (2011)
		$\ln k_{\text{rate}} = 11.54-(8690/T_{\text{K}})$	Romanek et al. (2011)
		$\Omega = \frac{[Ca^{2+}][CO_3^{2-}]}{K_{\text{SP}}}$	Definition
Sp	Reactive surface area (m^2/kg-soln)	Adjustable parameter	0.01 to 1000
F^*_{spr}	Spring DIC flux (moles/s)	$F^*_{\text{spr}} = F_{\text{spr}} \cdot [\text{DIC}]_{\text{spr}}$	-
F^*_{cr}	Creek DIC flux (moles/s)	$F^*_{\text{cr}} = F_{\text{cr}} \cdot [\text{DIC}]_{\text{cr}}$	-
F^*_{atm}	Atmospheric DIC flux (moles/s)	$F^*_{\text{atm}} = J_{\text{atm}} \cdot \text{S}A_{\text{pool}}$	-
$F^*_{\text{CaCO}_3}$	Carbonate DIC flux (moles/s)	$F^*_{\text{CaCO}_3} = J_{\text{CaCO}_3} \cdot \text{Sp}$	-
Part II: Reaction rate constants			
χ	Fraction of HCO_3^- in EIC	$\chi = \left(1+\frac{K_2}{[H^+]}\right)^{-1}$	K_2 from Millero et al. (2006)
k_{+1}	Rate const. CO_2 hydration (s^{-1})	$\log_{10} k_{+1} = 329.85 - 110.541\log_{10}(T_K) - \frac{17265.4}{T_K}$	Pinsent et al. (1956) Uchikawa and Zeebe (2012)

k_{-1}	Rate const. CO$_2$ dehydration (M^{-1}s^{-1})	$k_{-1}=k_{+1}/K_1$	K_1 from Millero et al. (2006)
k_{+4}	Rate const. CO$_2$ hydroxylation (M^{-1}s^{-1})	$\log_{10} k_{+4} = 13.635 - \frac{2895}{T_K}$	Pinsent et al. (1956) Uchikawa and Zeebe (2012)
k_{-4}	Rate const. CO$_2$ dehydroxylation (s^{-1})	$k_{-4} = k_{+4} \cdot \left(\frac{K_\mathrm{w}}{K_1}\right)$	K_w from DOE (1994)

Table 6 (cont'd). Constants and parameters used in the model

Symbol	**Meaning**	**Value**	**Reference/Note**
Part III: Isotopic parameters			
r_W	$^{18}O/^{16}O$ ratio of H_2O	0.00199377	$\delta^{18}O_{VSMOW}$=-5.7
r_{CO2}	$^{18}O/^{16}O$ ratio of CO_2	-	Isotope ratio
r_{EIC}	$^{18}O/^{16}O$ ratio of EIC	-	Isotope ratio
R_{CO2}	$[C^{18}OO]/[CO_2]$	$2r_{CO2}$	Isotopologue ratio
R_{EIC}	$[^{18}EIC]/[^{16}EIC]$	$3r_{EIC}$	Isotopologue ratio
⍰⍰χ	Fraction of $H^{13}CO_3^-$ in ^{13}EIC	$^{13}\chi = \left(1 + \dfrac{K_2 \cdot {}^{13}\alpha_{CO_3^{2-}/HCO_3^-}}{[H^+]}\right)^{-1}$	-
⍰8χ	Fraction of $HC^{18}OO_2^-$ in ^{18}EIC	$^{18}\chi = \left(1 + \dfrac{K_2 \cdot {}^{18}\alpha_{CO_3^{2-}/HCO_3^-}}{[H^+]}\right)^{-1}$	-
k'_{+1}	Rate const. for $^{13}CO_2$ hydration (s^{-1})	$k'_{+1}/k_{+1} = 0.987$	Zeebe & W-G (2001)
k'_{-1}	Rate const. for $^{13}CO_2$ dehydration ($M^{-1}s^{-1}$)	$k'_{+1}/k'_{-1} = K_1 \cdot {}^{13}\alpha_{HCO_3^-/CO_{2\,(aq)}}$	Equilibrium constraint
k'_{+4}	Rate const. for $^{13}CO_2$ hydrox. ($M^{-1}s^{-1}$)	$k'_{+4}/k_{+4} = 0.9829$	This study
k'_{-4}	Rate const. for $^{13}CO_2$ dehydrox. (s^{-1})	$k'_{+4}/k'_{-4} = K_1/K_W \cdot {}^{13}\alpha_{HCO_3^-/CO_{2\,(aq)}}$	Equilibrium constraint
a_{+1}, b_{+1}	Rate const.s for hydration ($M^{-1}s^{-1}$)	$a_{+1}/k_{+1} = 1.0000$ $b_{+1}/k_{+1} = 0.9812$	Yumol et al. (2020)†
a_{-1}, b_{-1}	Rate const.s for dehydration ($M^{-1}s^{-1}$)	$a_{+1}/k_{+1} = K_1 \cdot \alpha_{HCO_3^-/H_2O}$ $b_{+1}/k_{+1} = K_1 \cdot \alpha_{HCO_3^-/CO_2}$	Equilibrium constraint Equilibrium constraint
a_{+4}, b_{+4}	Rate const.s for hydrox. ($M^{-1}s^{-1}$)	$a_{+4}/k_{+4} = 0.9988$ $b_{+4}/k_{+4} = 1.0000$	This study‡ This study‡
a_{-4}, b_{-4}	Rate const.s for dehydrox. (s^{-1})	$a_{+4}/k_{+4} = \dfrac{K_1}{K_W} \cdot \dfrac{\alpha_{HCO_3^-/H_2O}}{\alpha_{OH^-/H_2O}}$ $b_{+4}/k_{+4} = \dfrac{K_1}{K_W} \cdot \alpha_{HCO_3^-/CO_2}$	Equilibrium constraint Equilibrium constraint
$^{13}R_{EIC(hydrox)}$	Composition of hydroxylated CO_2	18‰ lighter than $CO_{2(atm)}$	This study
$^{18}R_{EIC(hydrox)}$	Composition of hydroxylated CO_2	7.1‰ lighter than 'CO_2+OH^-'	This study

E_C	Calcite-$\mathrm{CO_3^{2-}}$ equilibration index	$E_c = \Omega^{-n_2},\ n_2 = 0.2$	Devriendt et al. (2017)
$^{13}\alpha_{\mathrm{C/CO_3^{2-}}}$	Growth rate-dependent isotopic fractionation	$\dfrac{^{13}\alpha_\mathrm{f}}{1+E_c\left(\dfrac{^{13}\alpha_\mathrm{f}}{^{13}\alpha_\mathrm{eq}}-1\right)}$ where $^{13}\alpha_\mathrm{f} = 1.0000$ and $^{13}\alpha_\mathrm{eq} = 1.0032$	Devriendt et al. (2017) DePaolo (2011) Watkins and Hunt (2014)
$^{18}\alpha_{\mathrm{C/CO_3^{2-}}}$	Growth rate-dependent isotopic fractionation	$\dfrac{^{18}\alpha_\mathrm{f}}{1+E_c\left(\dfrac{^{18}\alpha_\mathrm{f}}{^{18}\alpha_\mathrm{eq}}-1\right)}$ where $^{18}\alpha_\mathrm{f} = 0.9995$ and $^{18}\alpha_\mathrm{eq} = 1.0057$	Devriendt et al. (2017) DePaolo (2011)
$^{13}\alpha_{\mathrm{c/EIC}}$	Growth rate-dependent isotopic fractionation	$^{13}\alpha_{\mathrm{C/CO_3^{2-}}} \cdot \left(1-{}^{13}\chi\right)/\left(1-\chi\right)$	-
$^{18}\alpha_{\mathrm{c/EIC}}$	Growth rate-dependent isotopic fractionation	$^{18}\alpha_{\mathrm{C/CO_3^{2-}}} \cdot \left(1-{}^{18}\chi\right)/\left(1-\chi\right)$	-

---

†These values yield a bulk KFF that is consistent with Yumol et al. (2020)

‡These values yield a bulk KFF the is consistent with ‘this study’ in Table 7.

Table 7. Compilation of CO_2 hydroxylation KFF’s

						□^{13}C (‰ VPDB)				Carbon KFF		□^{18}O (‰ VSMOW)						Oxygen bulk KFF*			
reference	**study type**	**mineral**	**T (°C)**	**±**	**pH**	**$CO_{2(g)}$**	**±**	**mineral**	**±**	**vs $CO_{2(aq)}$[h]**	**±**	**H_2O**	**±**	**$CO_{2(g)}$**	**±**	**mineral**	**±**	**vs '$CO_{2(aq)}$ + OH^-'[k]**	**±**	**vs '$CO_{2(aq)}$ + H_2O'[k]**	**±**
Craig (1953)	Lab.	witherite	20	3	?	-9.1	0.1	-23.1	0.1	-13.7[i]	0.1	-	-	-	-	-	-	-	-	-	-
Usdowski & Hoefs (1986)	Lab.	witherite	18	1	10.0	-7.7[a]	0.3	-25.7	0.4	-17.0	0.5	-	-	-	-	-	-	-	-	-	-
Clark et al. (1992)	Lab.	witherite	22	2	>11.5	-10.5	0.4	-25.0	1.0	-13.9[i]	1.1	-6.7	0.1	36.6	0.3	6.8	1.0	-8.5	1.4	-15.0	0.2
Clark et al. (1992)	Lab.	witherite	22	2	12.8	-45.2	0.1	-61.3	0.1	-16.2[i]	0.1	-11.9	0.1	11.1	0.1	-11.2	0.1	-7.9	0.8	-14.5	0.1
Dietzel et al. (2009)	Lab.	calcite	5	1	10.5	-	-	-	-	-	-	-9.6	0.1	35.7[j]	0.1	3.4	0.1	-10.0	0.9	-16.8	0.1
Böttcher (2018)	Lab.	witherite	4	1	12.4	-8.6[b]	0.5	-21.4	0.1	-11.8	0.5	-7.0	0.1	30.9[b]	1.0	8.3	0.1	-2.8	1.5	-9.8	0.7
Böttcher (2018)	Lab.	witherite	21	1	12.4	-8.6[b]	0.5	-25.3	0.1	-15.8	0.5	-7.0	0.1	30.9[b]	1.0	10.0	0.1	-1.5	1.4	-8.1	0.7
Clark et al. (1992)	Field	calcite	28	6	11.5	-7.5	1.1	-24.5[c]	0.2	-17.0	1.1	-0.5	0.1	31.1[b]	0.5	14.3[c]	0.9	0.4	1.4	-6.2	0.4
Clark et al. (1992)	Field	calcite	28	6	11.5	-7.5	1.1	-25.3[d]	0.7	-16.9	1.3	-0.9	0.1	31.1[b]	0.5	13.5[d]	0.1	-0.3	1.0	-6.8	0.4
Mervine et al. (2014)	Field	calcite	28	6	11.0	-8.6[b]	0.2	-26.5[e]	0.3	-17.0	0.3	-0.5	1.5	31.1[b]	0.5	14.4[e]	0.4	0.5	1.1	-6.0	0.8
Falk et al. (2016)	Field	arag. & calcite	27	5	11.7	-8.6[b]	0.2	-26.8[f]	0.6	-17.2	0.6	0.1	1.0	31.1[b]	0.5	14.0[f]	0.4	0.0	1.1	-6.6	0.7
this study	Field	arag. & calcite	17	1	11.0	-8.6[b]	0.4	-26.6[g]	0.7	-17.1	0.8	-5.7	1.2	30.9[b]	1.0	11.4[g]	0.4	-0.4	1.5	-7.1	1.1

*Note: KFFs are expressed as e = (a-1)1000

[a] Keeling et al. (2001), station La Jolla (CA, USA)

[b] NOAA CO_2 global network station closest to study site (incl. 2017 Ochsenkopf, Germany; 2007-2012 Ketura, Israel; 2007-2012 Kaashidhoo, Maldives; 2013-2018 Trinidad Head, USA)

[c] average modern crust 'NJ' samples

[d] average modern crust 'clinic' samples

[e] average of two lowest 'crust' samples

[f] average of 'WHOI surface film' samples

[g] average 'BSC floes' samples

[h] $CO2_{(aq)}$-$CO_{2(g)}$ carbon fractionation of 1.1‰ from Vogel et al. (1970)

[i] corrected for distillation effect

[j] CO_2-H_2O isotopic equilibrium assumed

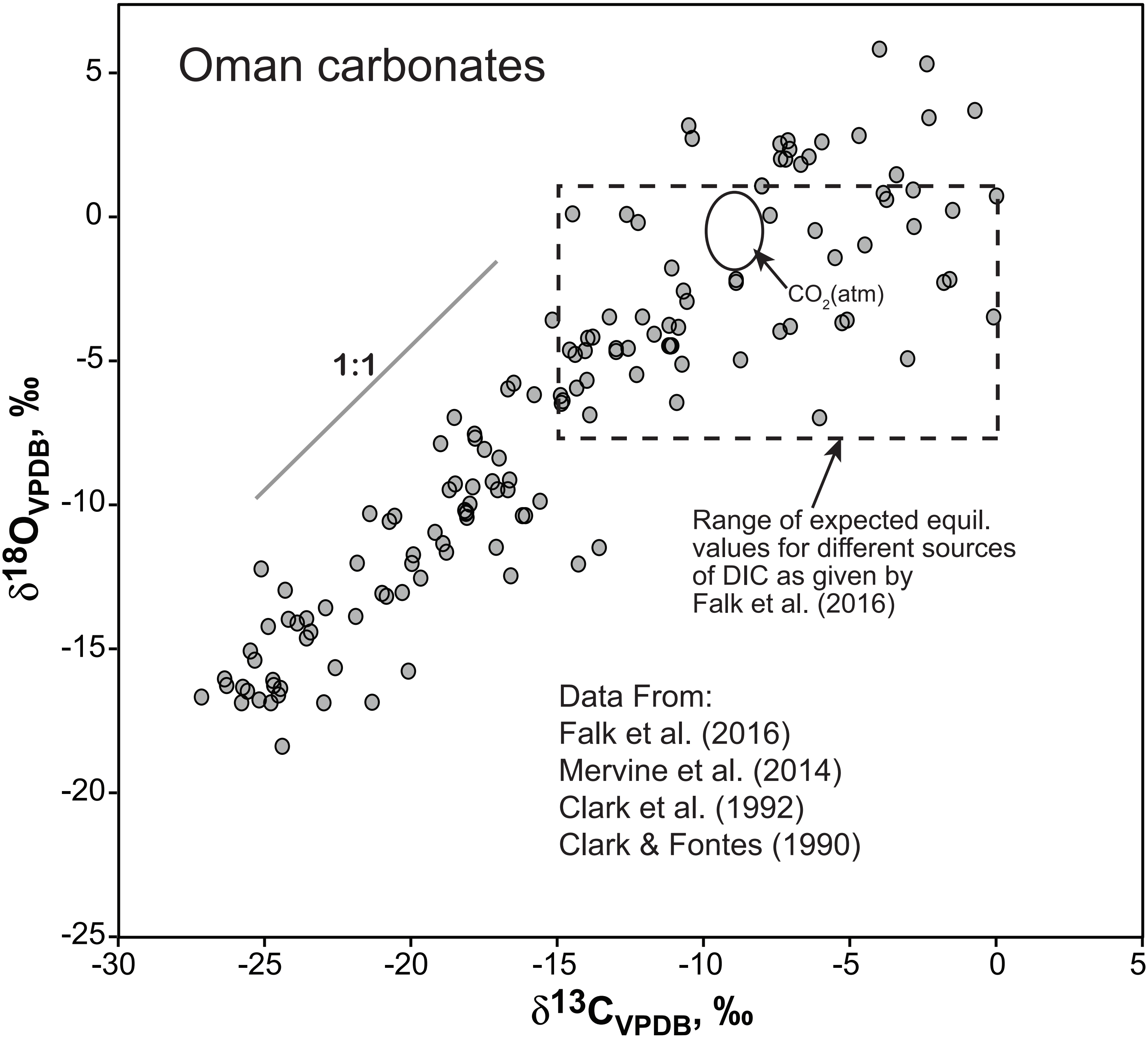
Oman carbonates
1:1
CO$_2$(atm)
Range of expected equil. values for different sources of DIC as given by Falk et al. (2016)
Data From:
Falk et al. (2016)
Mervine et al. (2014)
Clark et al. (1992)
Clark & Fontes (1990)
$\delta^{18}O_{VPDB}$, ‰
$\delta^{13}C_{VPDB}$, ‰
5
0
-5
-10
-15
-20
-25
-30
-25
-20
-15
-10
-5
0
5

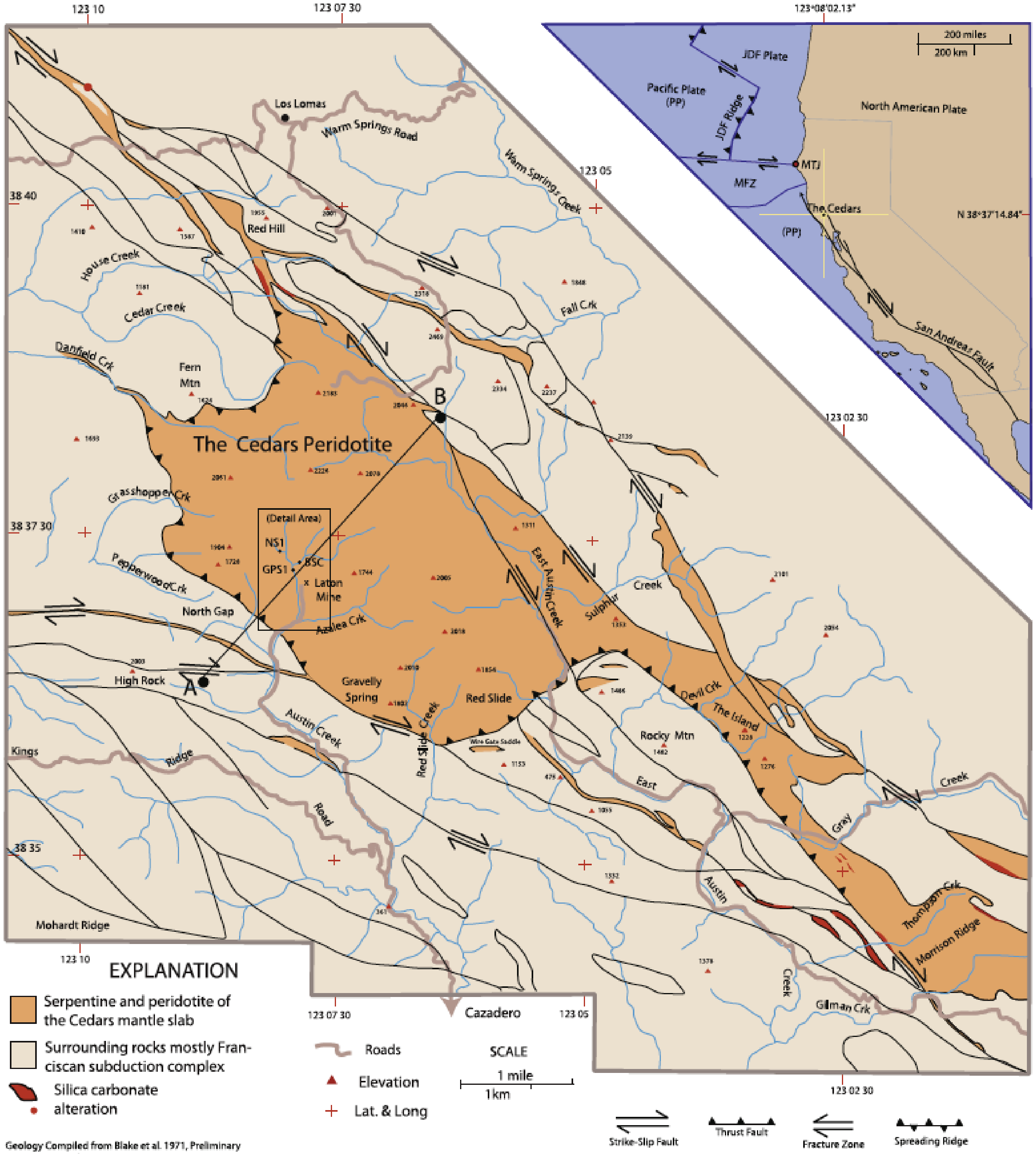

EXPLANATION

🟧	Serpentine and peridotite of the Cedars mantle slab
☐	Surrounding rocks mostly Franciscan subduction complex
🟥 ●	Silica carbonate alteration
〰	Roads
▲	Elevation
+	Lat. & Long

Geology Compiled from Blake et al. 1971, Preliminary Geologic Map of Western Sonoma County and Northernmost Marin County, California, USGS Open File Map

Fault features compiled by Robert Coleman, Stanford Geologic Survey, 1999.

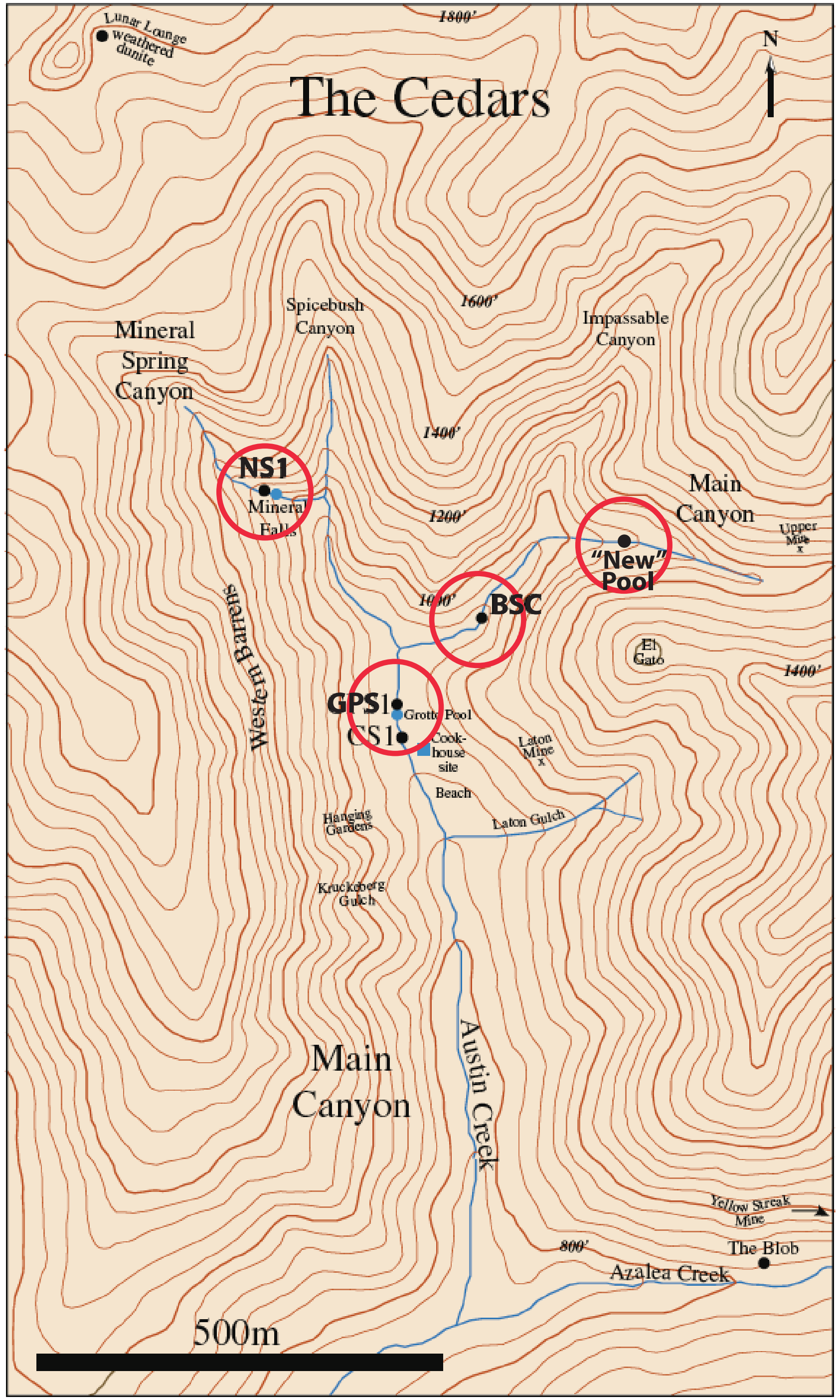

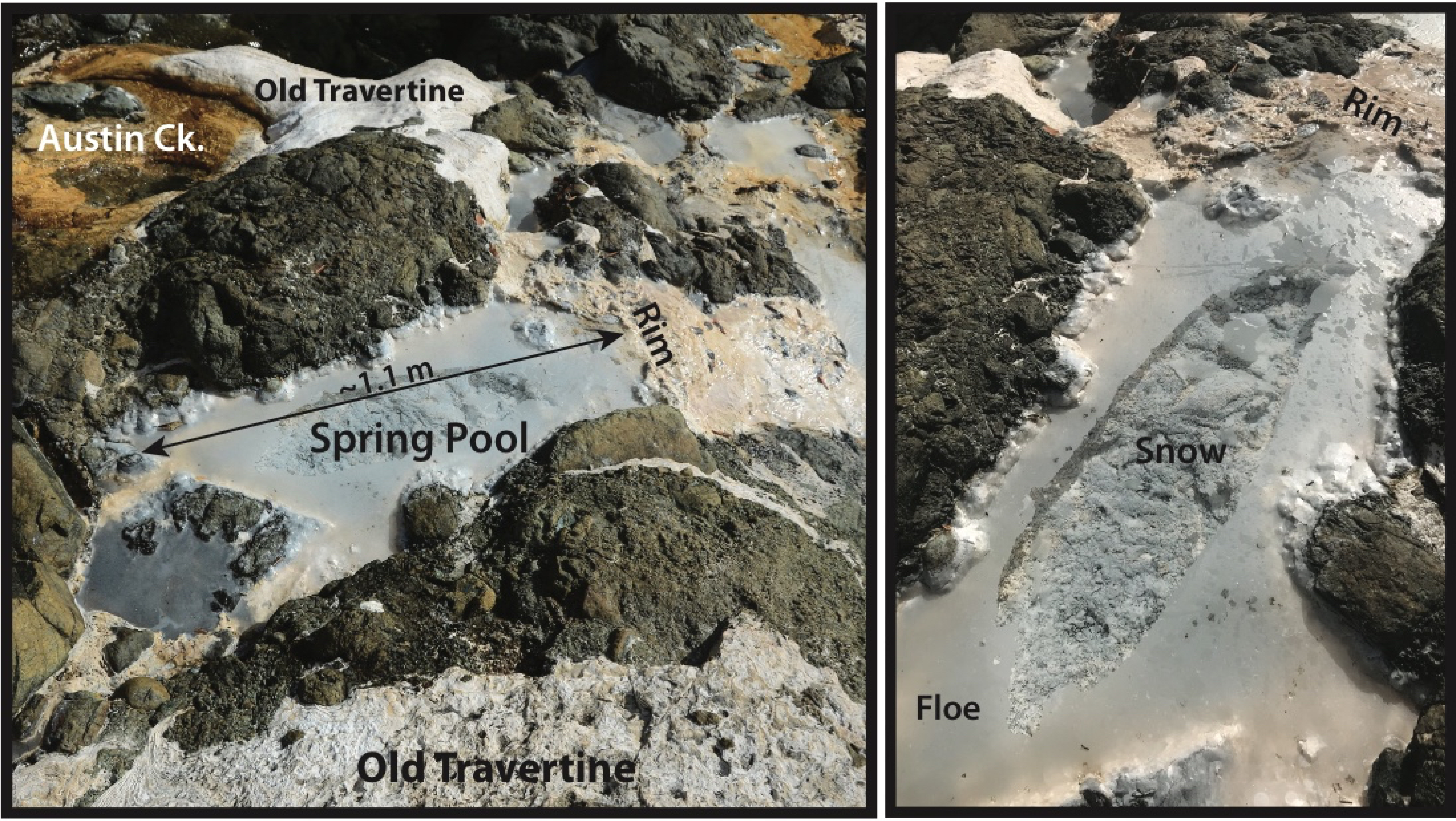
Old Travertine
Austin Ck.
Rim
~1.1 m
Spring Pool
Old Travertine
Rim
Snow
Floe

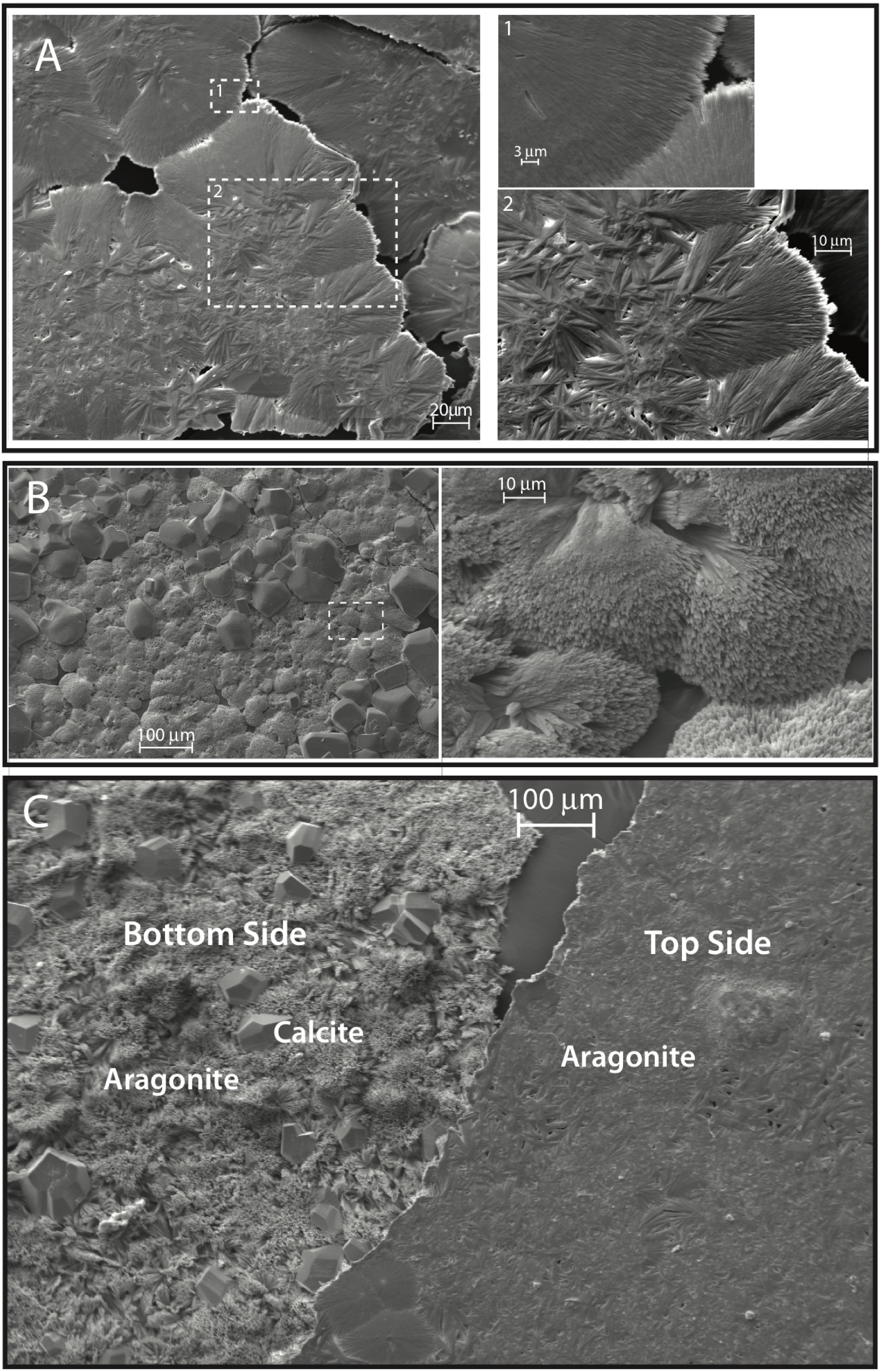
A
1
2
20µm
1
3 µm
2
10 µm
B
100 µm
10 µm
C
100 µm
Bottom Side
Top Side
Calcite
Aragonite
Aragonite

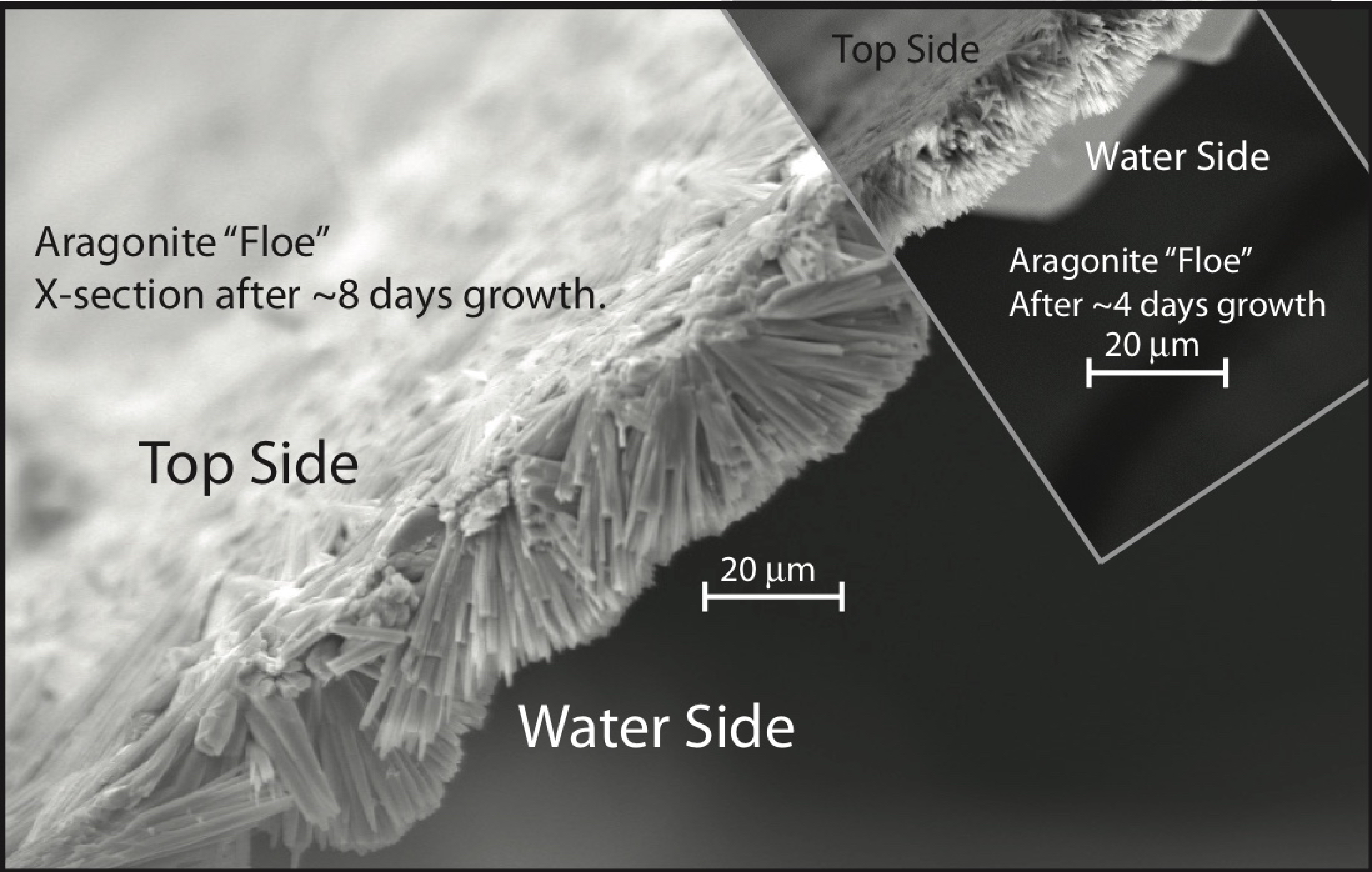
Aragonite "Floe"
X-section after ~8 days growth.
Top Side
Water Side
20 µm
Top Side
Water Side
Aragonite "Floe"
After ~4 days growth
20 µm

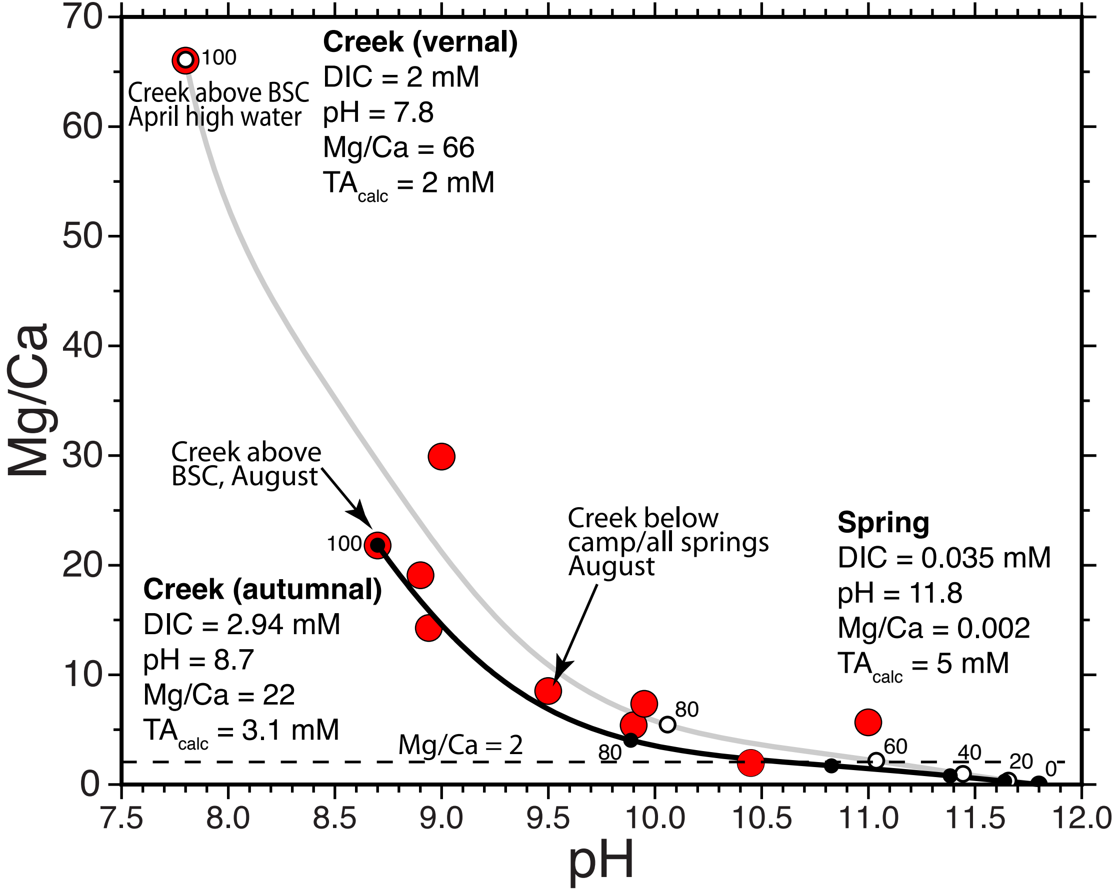
Creek (vernal)
DIC = 2 mM
pH = 7.8
Mg/Ca = 66
TA$_{calc}$ = 2 mM
100
Creek above BSC
April high water
Creek above BSC, August
100
Creek below camp/all springs August
Spring
DIC = 0.035 mM
pH = 11.8
Mg/Ca = 0.002
TA$_{calc}$ = 5 mM
Creek (autumnal)
DIC = 2.94 mM
pH = 8.7
Mg/Ca = 22
TA$_{calc}$ = 3.1 mM
Mg/Ca = 2
80
80
60
40
20
0
Mg/Ca
0
10
20
30
40
50
60
70
pH
7.5
8.0
8.5
9.0
9.5
10.0
10.5
11.0
11.5
12.0

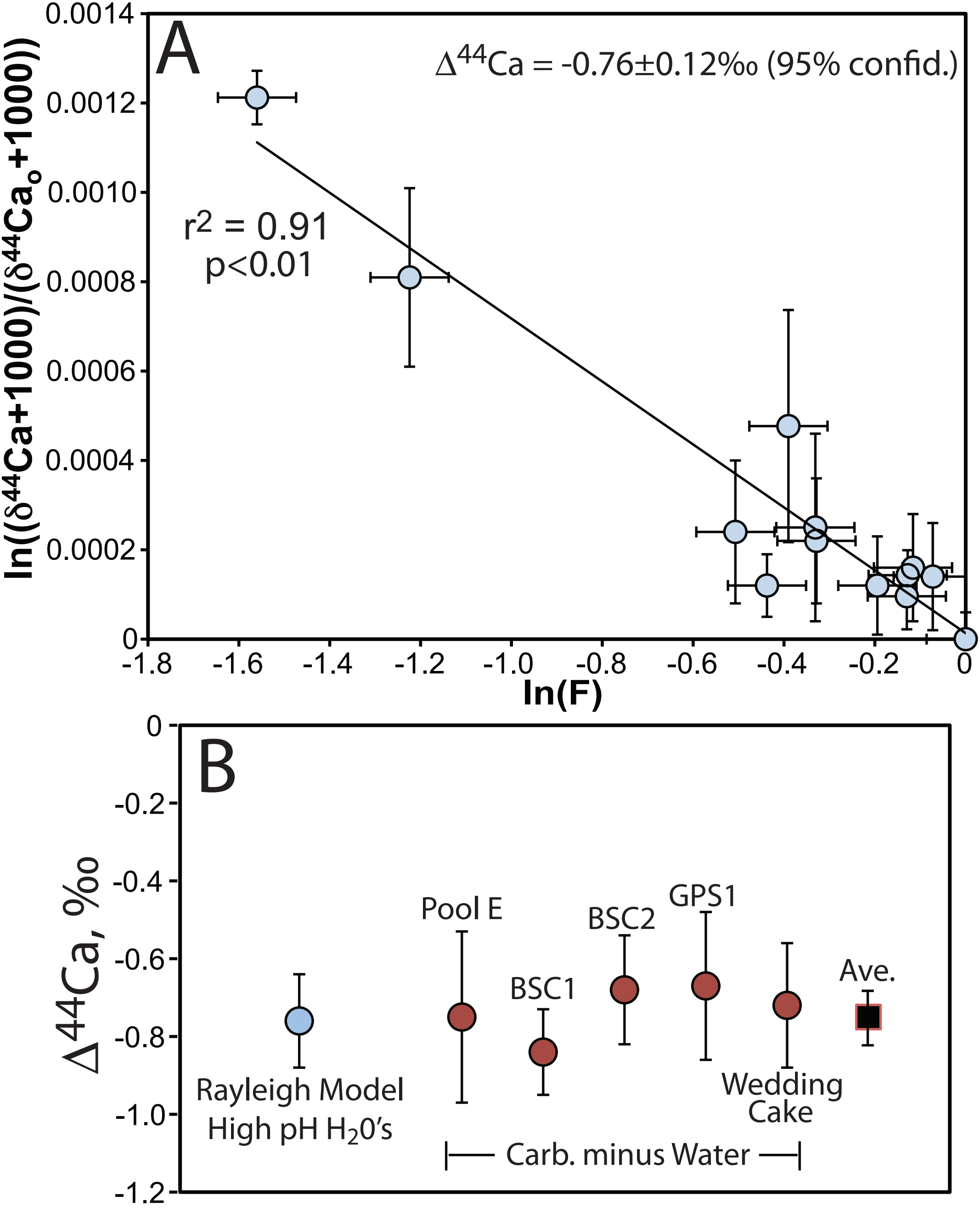
A
Δ44Ca = -0.76±0.12‰ (95% confid.)
r2 = 0.91
p<0.01
ln((δ44Ca+1000)/(δ44Cao+1000))
0.0014
0.0012
0.0010
0.0008
0.0006
0.0004
0.0002
0
-1.8
-1.6
-1.4
-1.2
-1.0
-0.8
-0.6
-0.4
-0.2
0
ln(F)
B
Δ44Ca, ‰
0
-0.2
-0.4
-0.6
-0.8
-1.0
-1.2
Rayleigh Model
High pH H20's
Pool E
BSC1
BSC2
GPS1
Wedding
Cake
Ave.
Carb. minus Water

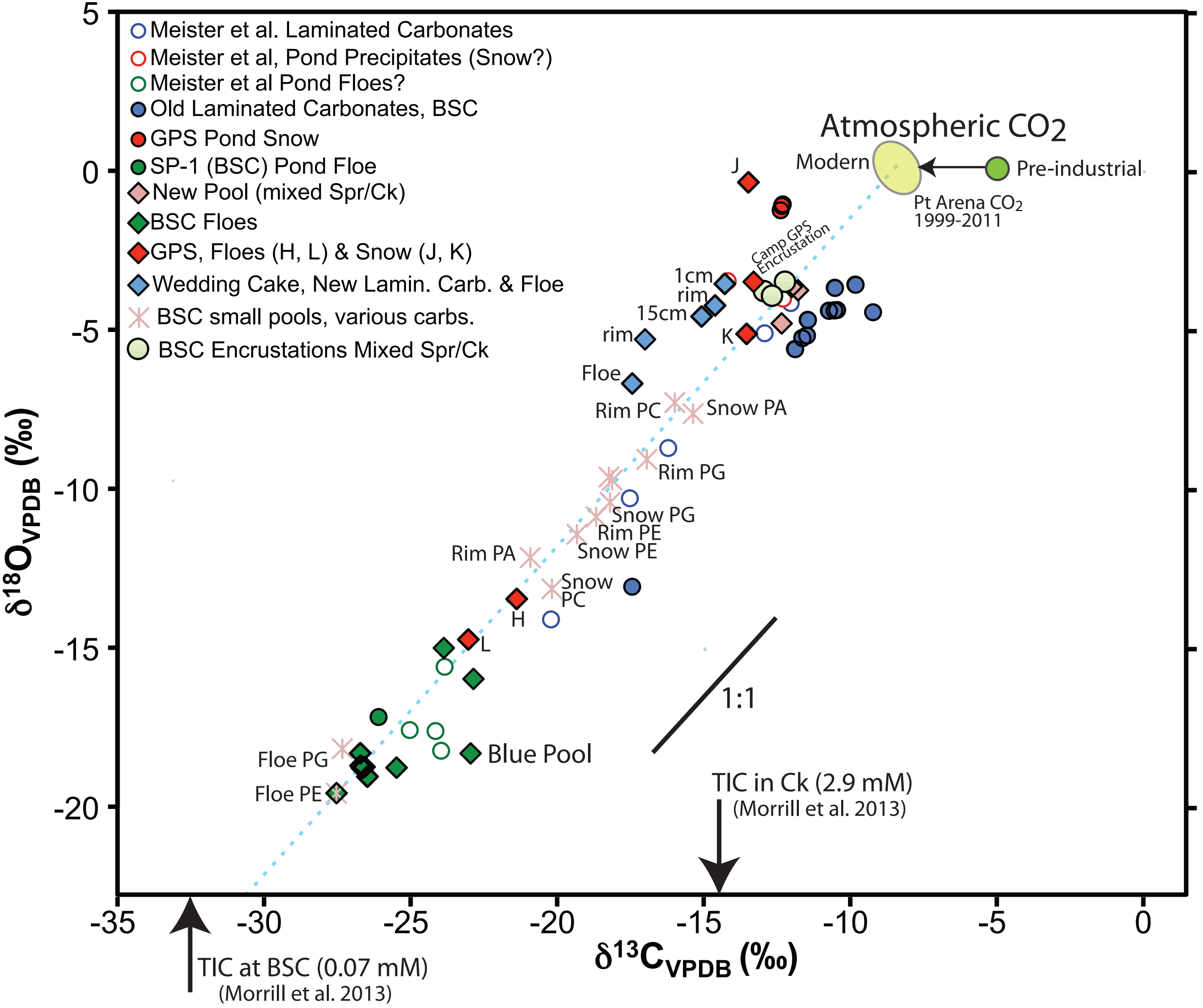
○ Meister et al. Laminated Carbonates
○ Meister et al, Pond Precipitates (Snow?)
○ Meister et al Pond Floes?
● Old Laminated Carbonates, BSC
● GPS Pond Snow
● SP-1 (BSC) Pond Floe
◆ New Pool (mixed Spr/Ck)
◆ BSC Floes
◆ GPS, Floes (H, L) & Snow (J, K)
◆ Wedding Cake, New Lamin. Carb. & Floe
✳ BSC small pools, various carbs.
● BSC Encrustations Mixed Spr/Ck
Atmospheric CO2
Modern
Pre-industrial
Pt Arena CO2
1999-2011
J
Camp GPS
Encrustation
1cm
rim
15cm
rim
K
Floe
Rim PC
Snow PA
Rim PG
Snow PG
Rim PE
Snow PE
Rim PA
Snow
PC
H
L
1:1
Floe PG
Floe PE
Blue Pool
TIC in Ck (2.9 mM)
(Morrill et al. 2013)
TIC at BSC (0.07 mM)
(Morrill et al. 2013)
5
0
-5
-10
-15
-20
-35
-30
-25
-20
-15
-10
-5
0
δ18OVPDB (‰)
δ13CVPDB (‰)

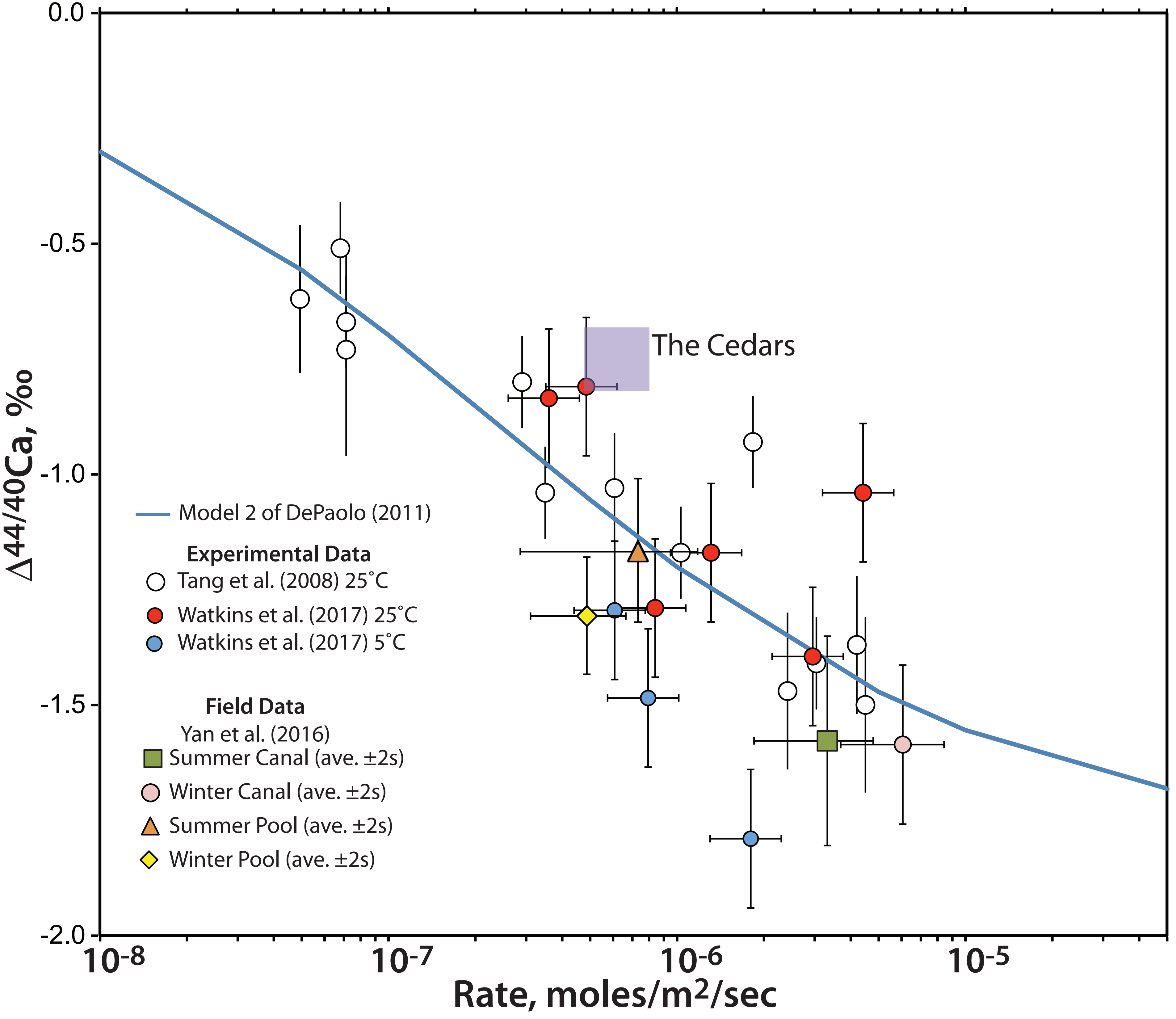
0.0
-0.5
-1.0
-1.5
-2.0
$\Delta^{44/40}$Ca, ‰
10^{-8}
10^{-7}
10^{-6}
10^{-5}
Rate, moles/m^2/sec
The Cedars
Model 2 of DePaolo (2011)
Experimental Data
Tang et al. (2008) 25˚C
Watkins et al. (2017) 25˚C
Watkins et al. (2017) 5˚C
Field Data
Yan et al. (2016)
Summer Canal (ave. ±2s)
Winter Canal (ave. ±2s)
Summer Pool (ave. ±2s)
Winter Pool (ave. ±2s)

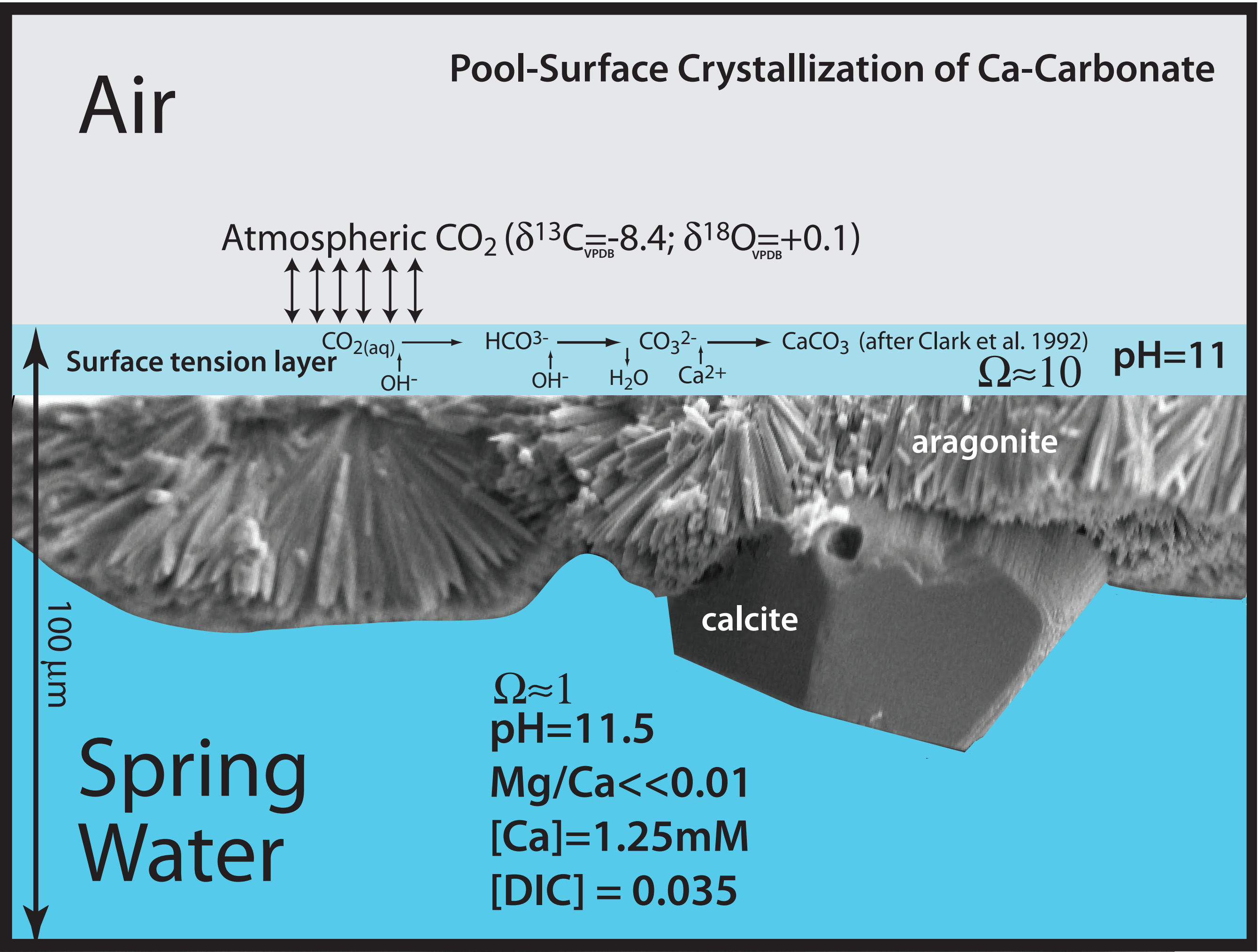
Pool-Surface Crystallization of Ca-Carbonate
Air
Atmospheric CO_2 ($\delta^{13}C_{VPDB}$=-8.4; $\delta^{18}O_{VPDB}$=+0.1)
Surface tension layer
$CO_{2(aq)} \rightarrow HCO^{3-} \rightarrow CO_3^{2-} \rightarrow CaCO_3$ (after Clark et al. 1992)
OH^-
OH^-
H_2O
Ca^{2+}
$\Omega \approx 10$
pH=11
aragonite
calcite
100 µm
$\Omega \approx 1$
pH=11.5
Mg/Ca<<0.01
[Ca]=1.25mM
[DIC] = 0.035
Spring Water

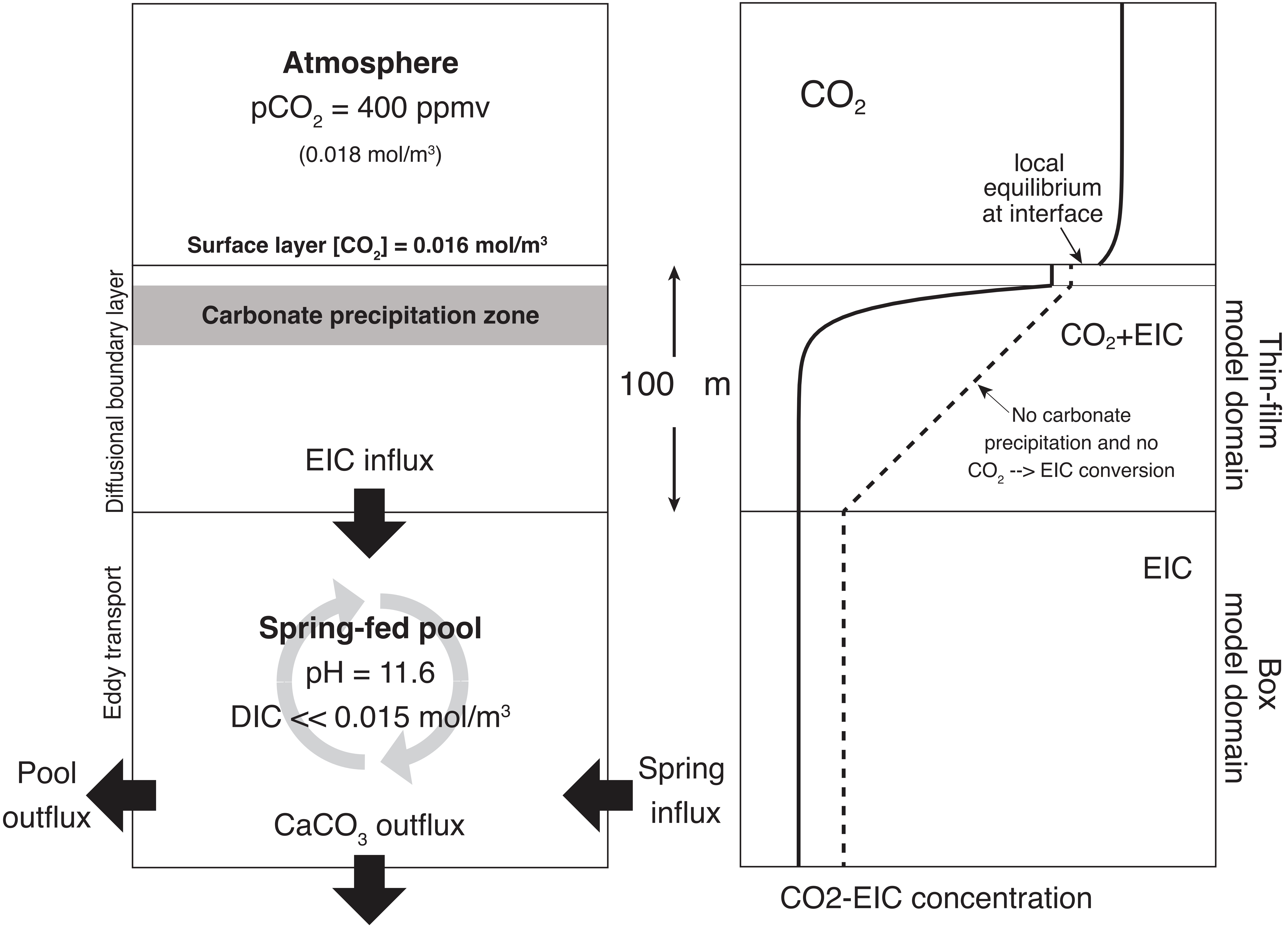
Atmosphere
pCO$_2$ = 400 ppmv
(0.018 mol/m^3)
Surface layer [CO$_2$] = 0.016 mol/m^3
Diffusional boundary layer
Carbonate precipitation zone
EIC influx
Eddy transport
Spring-fed pool
pH = 11.6
DIC << 0.015 mol/m^3
Pool outflux
CaCO$_3$ outflux
Spring influx
100 m
CO$_2$
local equilibrium at interface
CO$_2$+EIC
No carbonate precipitation and no CO$_2$ --> EIC conversion
EIC
Thin-film model domain
Box model domain
CO2-EIC concentration

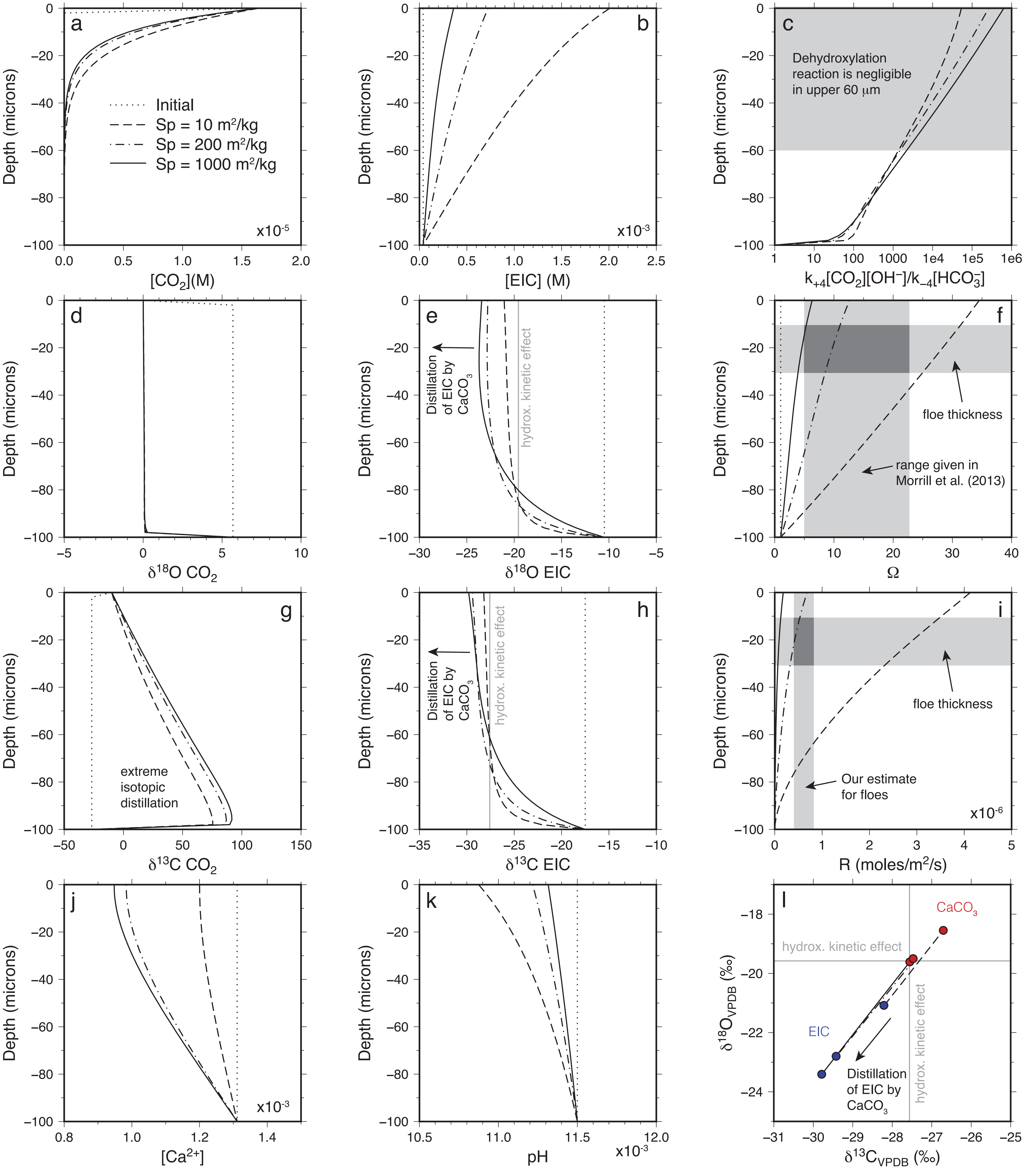
a
Depth (microns)
[CO$_2$](M)
x10^{-5}
Initial
Sp = 10 m^2/kg
Sp = 200 m^2/kg
Sp = 1000 m^2/kg
b
[EIC] (M)
x10^{-3}
c
Dehydroxylation reaction is negligible in upper 60 μm
k$_{+4}$[CO$_2$][OH$^-$]/k$_{-4}$[HCO$_3^-$]
d
δ^{18}O CO$_2$
e
Distillation of EIC by CaCO$_3$
hydrox. kinetic effect
δ^{18}O EIC
f
floe thickness
range given in Morrill et al. (2013)
Ω
g
extreme isotopic distillation
δ^{13}C CO$_2$
h
Distillation of EIC by CaCO$_3$
hydrox. kinetic effect
δ^{13}C EIC
i
floe thickness
Our estimate for floes
x10^{-6}
R (moles/m^2/s)
j
[Ca^{2+}]
x10^{-3}
k
pH
x10^{-3}
l
CaCO$_3$
hydrox. kinetic effect
EIC
Distillation of EIC by CaCO$_3$
hydrox. kinetic effect
δ^{18}O$_{VPDB}$ (‰)
δ^{13}C$_{VPDB}$ (‰)

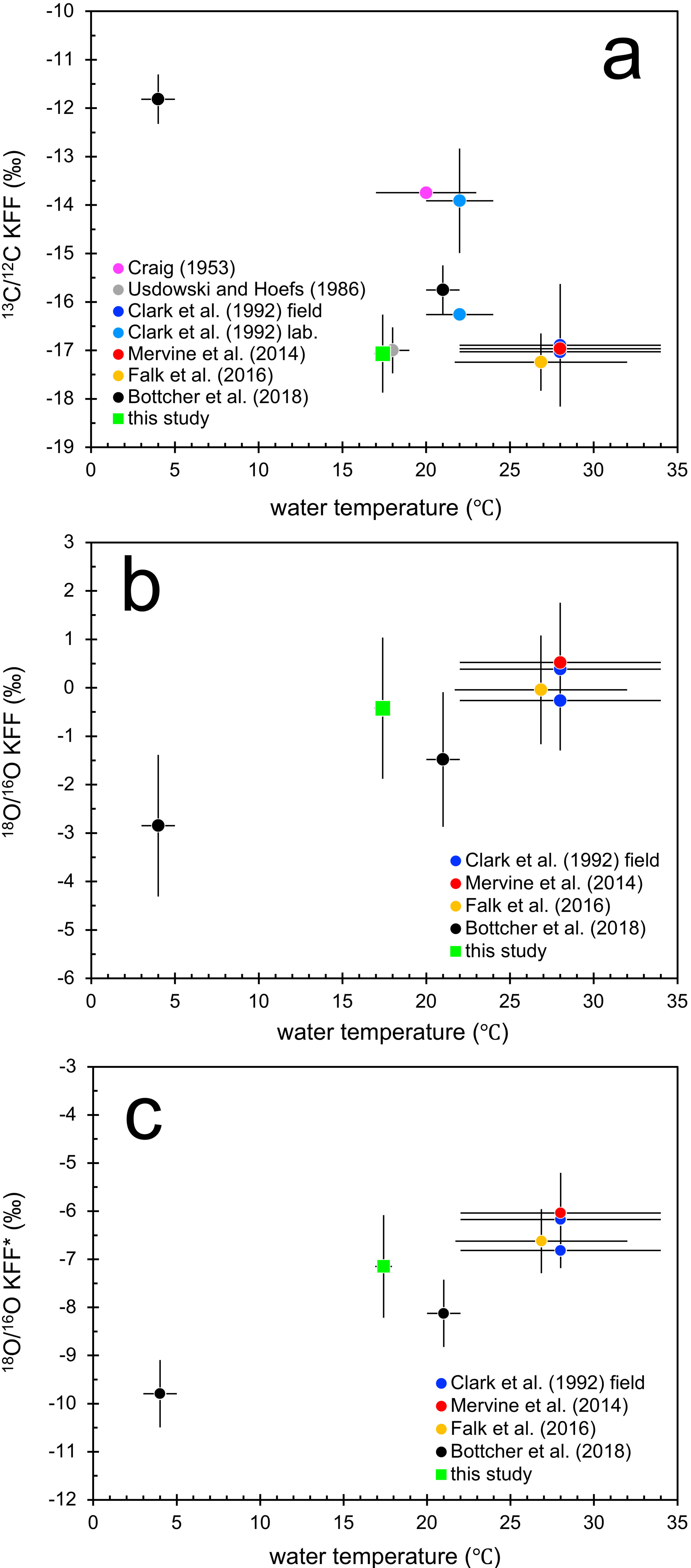
a
¹³C/¹²C KFF (‰)
-10
-11
-12
-13
-14
-15
-16
-17
-18
-19
0
5
10
15
20
25
30
35
water temperature (℃)
Craig (1953)
Usdowski and Hoefs (1986)
Clark et al. (1992) field
Clark et al. (1992) lab.
Mervine et al. (2014)
Falk et al. (2016)
Bottcher et al. (2018)
this study
b
¹⁸O/¹⁶O KFF (‰)
3
2
1
0
-1
-2
-3
-4
-5
-6
0
5
10
15
20
25
30
35
water temperature (℃)
Clark et al. (1992) field
Mervine et al. (2014)
Falk et al. (2016)
Bottcher et al. (2018)
this study
c
¹⁸O/¹⁶O KFF* (‰)
-3
-4
-5
-6
-7
-8
-9
-10
-11
-12
0
5
10
15
20
25
30
35
water temperature (℃)
Clark et al. (1992) field
Mervine et al. (2014)
Falk et al. (2016)
Bottcher et al. (2018)
this study

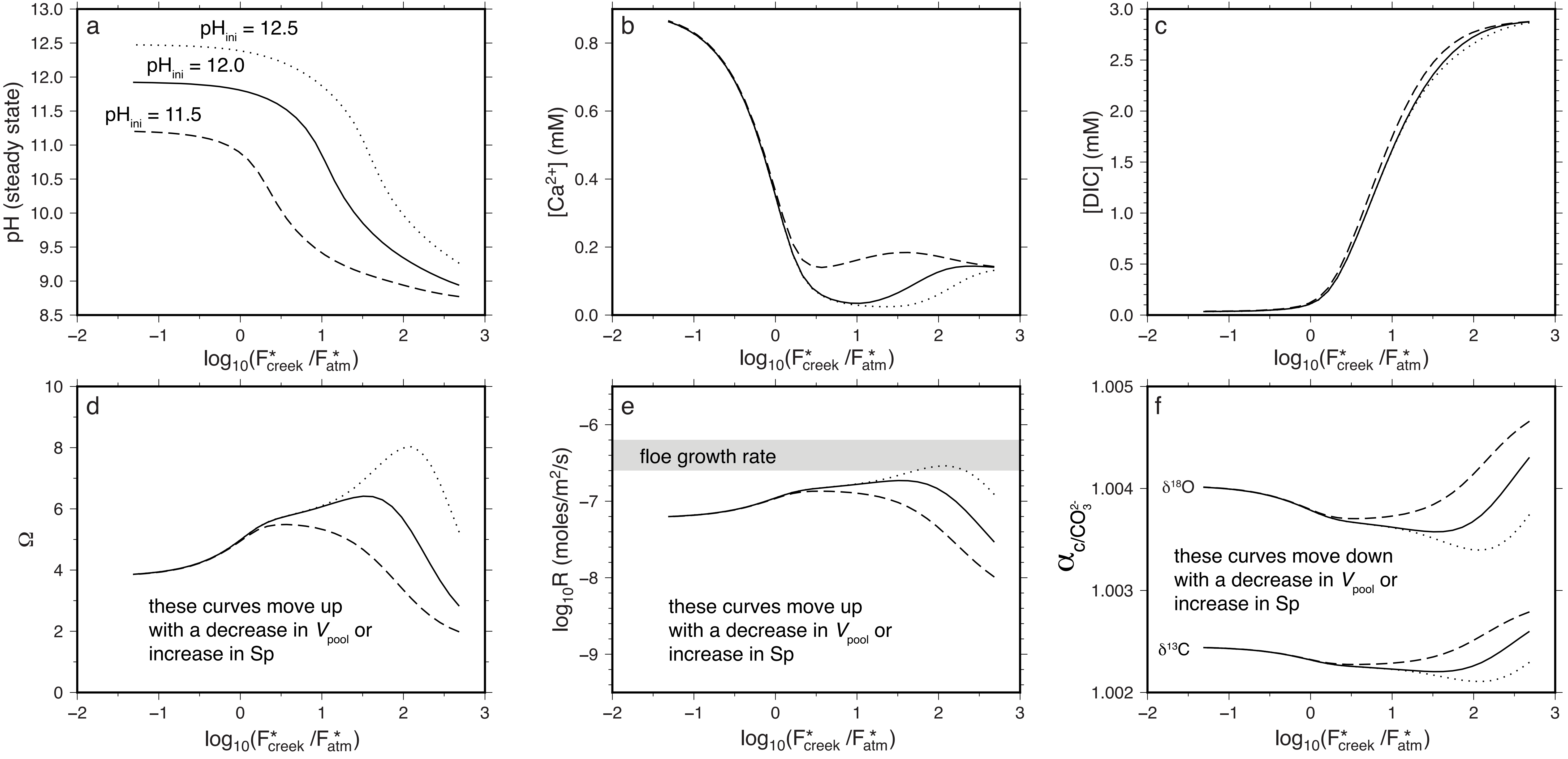
a
pH (steady state)
pH$_{ini}$ = 12.5
pH$_{ini}$ = 12.0
pH$_{ini}$ = 11.5
13.0
12.5
12.0
11.5
11.0
10.5
10.0
9.5
9.0
8.5
−2
−1
0
1
2
3
log$_{10}$(F$^*_{creek}$ /F$^*_{atm}$)
b
[Ca^{2+}] (mM)
0.8
0.6
0.4
0.2
0.0
−2
−1
0
1
2
3
log$_{10}$(F$^*_{creek}$ /F$^*_{atm}$)
c
[DIC] (mM)
3.0
2.5
2.0
1.5
1.0
0.5
0.0
−2
−1
0
1
2
3
log$_{10}$(F$^*_{creek}$ /F$^*_{atm}$)
d
Ω
these curves move up with a decrease in V_{pool} or increase in Sp
10
8
6
4
2
0
−2
−1
0
1
2
3
log$_{10}$(F$^*_{creek}$ /F$^*_{atm}$)
e
log$_{10}$R (moles/m^2/s)
floe growth rate
these curves move up with a decrease in V_{pool} or increase in Sp
−6
−7
−8
−9
−2
−1
0
1
2
3
log$_{10}$(F$^*_{creek}$ /F$^*_{atm}$)
f
$\alpha_{c/CO_3^{2-}}$
δ^{18}O
δ^{13}C
these curves move down with a decrease in V_{pool} or increase in Sp
1.005
1.004
1.003
1.002
−2
−1
0
1
2
3
log$_{10}$(F$^*_{creek}$ /F$^*_{atm}$)

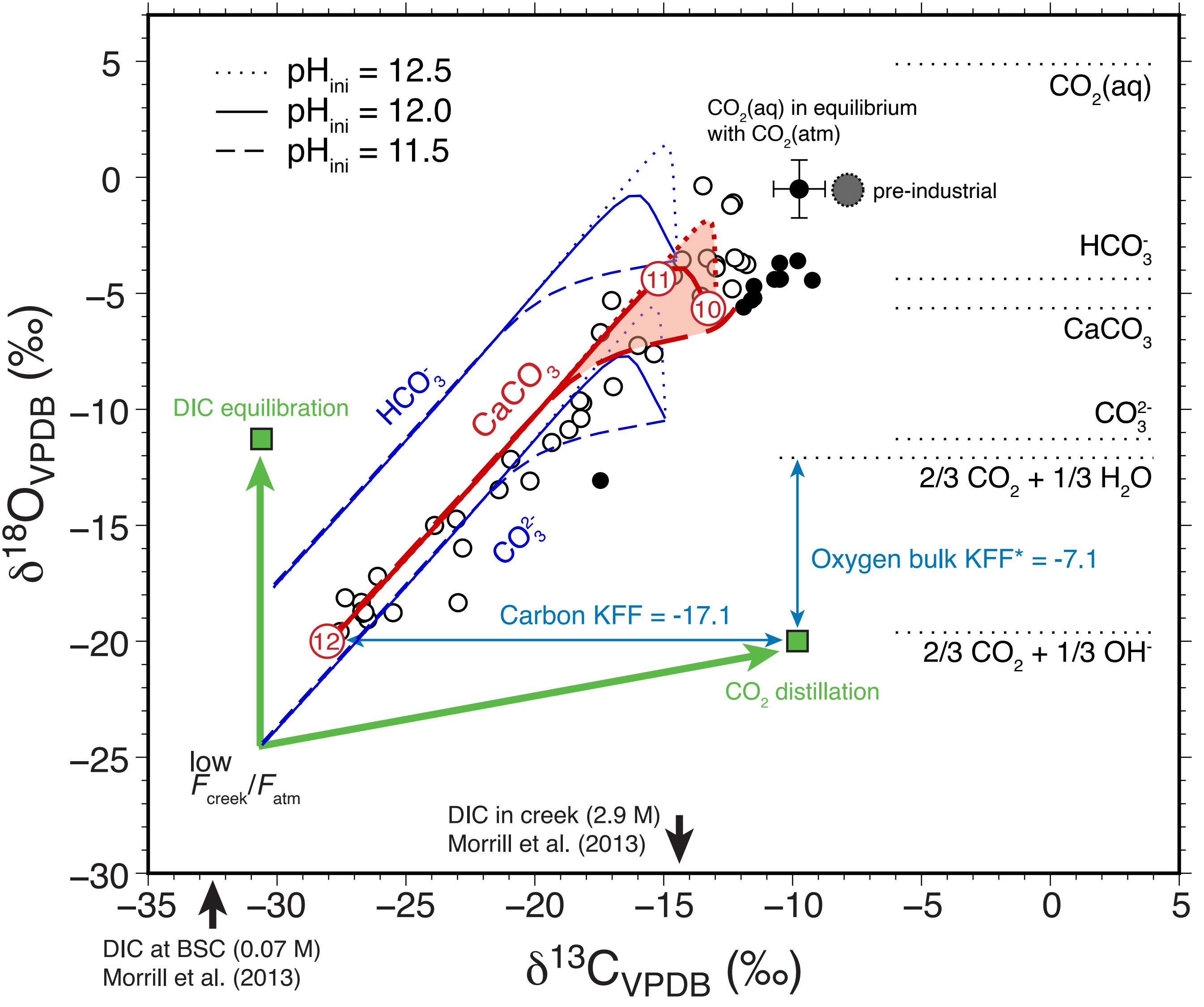
pH$_{ini}$ = 12.5
pH$_{ini}$ = 12.0
pH$_{ini}$ = 11.5
CO$_2$(aq) in equilibrium with CO$_2$(atm)
pre-industrial
CO$_2$(aq)
HCO$_3^-$
CaCO$_3$
CO$_3^{2-}$
2/3 CO$_2$ + 1/3 H$_2$O
2/3 CO$_2$ + 1/3 OH$^-$
DIC equilibration
HCO$_3^-$
CaCO$_3$
CO$_3^{2-}$
11
10
12
Oxygen bulk KFF* = -7.1
Carbon KFF = -17.1
CO$_2$ distillation
low F_{creek}/F_{atm}
DIC in creek (2.9 M) Morrill et al. (2013)
DIC at BSC (0.07 M) Morrill et al. (2013)
δ^{18}O$_{VPDB}$ (‰)
δ^{13}C$_{VPDB}$ (‰)
5
0
−5
−10
−15
−20
−25
−30
−35
−30
−25
−20
−15
−10
−5
0
5